This article has been accepted for publication in a future issue of this journal, but has not been fully edited. Content may change prior to final publication. Citation information: DOI 10.1109/ACCESS.2019.2959128, IEEE Access

IEEE Access
Multidisciplinary | Rapid Review | Open Access Journal

Digital Object Identifier

A Fast Sparse Recovery Algorithm via Resolution Approximation for LASAR 3D imaging

BOKUN TIAN, XIAOLING ZHANG(Member, IEEE), SHUNJUN WEI(Member, IEEE), JING MING, JUN SHI(Member, IEEE),LIANG LI,XINXIN TANG
University of Electronic Science and Technology of China,Chengdu , 611731, P.R.China

Corresponding author: Xiaoling Zhang (xlzhang@uestc.edu.cn)

This work was supported in part by the National Key R&D Program of China under Grant No. 2017YFB0502700 and in part by the National Natural Science Foundation of China under Grant No.61671113, 61501098, and 61571099.

ABSTRACT Compressed sensing (CS) algorithms are used for linear array synthetic aperture radar (LASAR) three-dimensional (3D) imaging. However, it is difficult to obtain imaging results with both high computational efficiency and promising imaging quality. Because of the high-dimensional matrix-operations, the computational complexity of several CS algorithms is huge such as the iterative adaptive approach (IAA), bayesian compressed sensing (BCS), and sparsity bayesian recovery via iterative minimum (SBRIM) algorithm. Besides, the greedy pursuit algorithms such as the orthogonal matching pursuit (OMP) algorithm cannot acquire ideal imaging results on account of the preset sparsity of the imaging scene. To solve the problem, we present a fast sparse recovery algorithm via resolution approximation (FSRARA) in this paper. Firstly, the whole imaging scene is divided into 3D scattering units with large spacing, and SBRIM algorithm is used to obtain its low-resolution imaging results quickly. Secondly, the low-resolution imaging results are conducted image segmentation by the fuzzy c-means (FCM) clustering algorithm to extract the possible targets' areas coarsely. Then we re-divide the imaging scene by higher imaging resolution and extract the possible targets' areas according to the coarsely possible targets' areas. FSRARA achieves improved computational efficiency with low-dimensional matrix-operations on the possible targets' areas instead of the high-dimensional one on the whole imaging scene. Meanwhile, FSRARA performs better in suppressing the false targets and sidelobe interference and improves the imaging quality than the SBRIM algorithm. Simulation and experimental results prove that FSRARA improves the computational efficiency by hundreds of times at most than SBRIM algorithm and its computational efficiency is higher than smoothed L_0 norm (SL0), IAA, and BCS algorithm. Besides, FSRARA improves the imaging quality compared with OMP, IAA, SL0, BCS, and SBRIM algorithms.

INDEX TERMS Compressed sensing, LASAR 3D imaging, Fast sparse recovery algorithm via resolution approximation, Image segmentation

I. INTRODUCTION

SYNTHETIC aperture radar (SAR) is a radar imaging technique with all-day, all-weather working capabilities, and has been successfully applied in both military and civil fields because of its high-resolution imaging ability. However, traditional SAR images only obtain the two dimensional (2D) targets' information on the Range-Doppler domain, and cannot reflect targets' information in the height dimension. How to obtain targets' three-dimensional (3D) imaging results has been the fascinating issue of SAR imaging technology, which leads to the emergence of several SAR 3D imaging technologies such as curvilinear SAR (CurSAR) [1], tomography SAR (TomoSAR) [2], and linear array SAR (LASAR) [3] recently. CurSAR synthesizes a curve array through the moving of one single antenna and combines the range compression technology to obtain the three-dimensional (3D) imaging resolution of the imaging scene. TomoSAR achieves the third-dimensional resolution by synthesizing a virtual aperture in the tomography direction with multiple parallel voyages. However, it is difficult to achieve the ideal curve trajectory and obtain high imaging resolution in CurSAR, and TomoSAR is limited by the multi-voyage parallel trajectory requirement. Meanwhile, both CurSAR

and TomoSAR can only obtain high-quality 3D imaging results under one working mode. Those shortcomings constrain the application of CurSAR and TomoSAR in 3D imaging seriously. LASAR [3] achieves 3D imaging resolution by the moving of linear array antenna and range compression technology. Different from CurSAR and TomoSAR, LASAR can achieve 3D high-quality imaging under different working modes such as downward-looking mode and forward-looking mode. However, LASAR faces many challenges to realize 3D imaging such as the huge antenna elements and the high-dimensional echo signal.

Sparse recovery algorithms via compressed sensing (CS) [4]– [7] theory have been widely researched because of their super-resolution imaging ability compared with the matched filter (MF) algorithm [8], and they can achieve high-quality imaging with the sampling rate of echo signal lower than the Nyquist sampling rate. Meanwhile, scholars have proposed several sparse recovery algorithms recently, such as orthogonal matching pursuit (OMP) algorithm [9]– [10], Bayesian compressed sensing (BCS) algorithm [11]– [12], iterative shrinkage/thresholding (IST) method [13], and the dictionary learning (DL) algorithm [14]. Zhang et.al [15] have proposed a Robust Flexible Discriminative Dictionary Learning method to improve the traditional DL algorithms' performance, and they also proposed a Locality-Constrained Projective Dictionary Learning (LC-PDL) [16] to reduce the computational cost of DL algorithms. And sparse reconstruction algorithms have been used in several areas such as the radar imaging, image feature extraction [17], and feature selection [18]– [19]. Besides, because of the sparsity of the SAR imaging scene, CS algorithms have been used for SAR imaging recently. In [20], a threshold gradient pursuit (TGP) algorithm was proposed for SAR 3D imaging, which uses the maximum-minimum ratio and changing rate of the scattering coefficients to replace the preset sparsity of the imaging scene. In [21], the iterative adaptive approach (IAA) was used for SAR imaging. In [22], the smoothed L_0 norm (SL0) algorithm was used for high-resolution Inverse SAR (ISAR) imaging by combining the cycle shift method and exploiting sparse apertures. In [23], an ISAR imaging algorithm based on sparse Bayesian learning (SBL) algorithm was proposed to achieve a sparser solution and select the parameters automatically. In [24], the sequential order one negative exponential (SOONE) function was used to measure the signal's sparsity. Meanwhile, a 2D gradient projection (GP)-SOONE algorithm was proposed for super-resolution ISAR imaging.

CS algorithms are used for LASAR 3D imaging because of the sparsity of the 3D imaging scene. In [25], a combination of polar formatting and L_1 regularization algorithm was proposed for downward-looking LASAR 3D sparse imaging. In [26], the BCS algorithm was used for reducing sidelobes in LASAR 3D imaging. In [27], a 3D CS algorithm was proposed to solve the couple effects between different directions in LASAR imaging by reconstructing the 2D sparse signals on overcomplete dictionaries with separable atoms directly. Besides, the sparsity bayesian recovery via iterative minimum (SBRIM) algorithm was proposed in [28] by setting the scattering coefficients of the imaging scene obey the exponential prior distribution, which achieves high-resolution imaging without the preset sparsity, and improves the imaging quality by reducing the preset parameters compared with BCS algorithm. However, the high-dimensional matrix-operations make the computational complexity of SBRIM algorithm very huge and limit its application.

CS algorithms obtain imaging results with higher quality at the expense of increased computational complexity compared with the MF [8] algorithm. Meanwhile, scholars have proposed several methods to reduce the reconstruction time of CS algorithms recently. To cut down the computational burden, article [29] introduced the SL0 algorithm into SAR sparse imaging. In [30], the whole scene was divided into several sub-scenes by the range profiles; and then the whole image was obtained by combining the reconstructed sub-scenes according to the range profile sub-patches. In [31], the equidistant slice split (ESS) algorithm was used to split the 3D imaging scene into several 2D equidistant slices along the range direction, and the 3D imaging results were obtained by combining the 2D image of every equidistant slice. Zhao et al [32] used the truncated singular value decomposition (TSVD) algorithm to decrease the computational complexity of LASAR 3D imaging. Meanwhile, according to the Fourier property of the measurement matrix and the Toeplitz structure of the covariance matrix, Zhang et al [33] proposed a fast IAA algorithm for scanning radar imaging. However, those algorithms except the fast IAA algorithm still conduct imaging of the whole imaging scene and cannot improve the computational efficiency of CS algorithms efficiently. Meanwhile, the measurement matrix in SAR imaging is not the Fourier matrix, the fast IAA algorithm is not suitable for high-quality imaging.

To improve the computational efficiency of CS algorithms, a fast sparse recovery algorithm via resolution approximation (FSRARA) is proposed in this paper. Firstly, the whole imaging scene is divided into 3D scattering units by a uniform spacing larger than the traditional imaging resolution of LASAR 3D imaging, and the SBRIM algorithm is used to obtain the 3D low-resolution imaging results of the whole imaging scene quickly. Secondly, we use the fuzzy c-means (FCM) [34] clustering algorithm to perform image segmentation on the preliminary imaging results to extract the possible targets' areas in the imaging scene coarsely. Then, we re-divide the imaging scene by smaller spacing and re-extract the possible targets' areas according to the coarsely possible targets' areas. Finally, we use the possible targets' areas to construct the measurement matrix and perform high-resolution imaging. Besides, the main contributions of FSRARA are shown as follows:

- Improve the computational efficiency significantly: FSRARA has converted the high-dimensional matrix-operations on the 3D imaging scene to the low-dimensional matrix-operations on the possible targets' areas. Meanwhile,

This article has been accepted for publication in a future issue of this journal, but has not been fully edited. Content may change prior to final publication. Citation information: DOI 10.1109/ACCESS.2019.2959128, IEEE Access

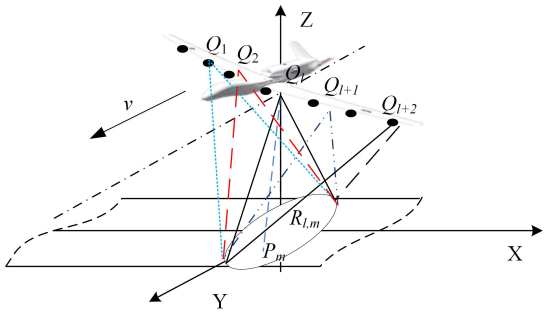

FIGURE 1. The geometric model of downward-looking LASAR

because of the 3D imaging scene's sparsity, the possible targets' areas are far less than the whole imaging scene. Therefore, FSRARA has improved the computational efficiency significantly compared with SBRIM algorithm.

• Improve the imaging quality: the influence of false targets or sidelobe interference are suppressed more effectively by constructing the measurement matrix by the possible targets' areas. Therefore, FSRARA has improved the imaging quality compared with SBRIM algorithm.

The remaining sections are arranged as follows: the 3D sparse imaging model of LASAR is introduced in section II; the FSRARA is proposed in section III; the performance of FSRARA is analyzed by simulation and experimental results in section IV; Section V proposes the main conclusions of the whole paper.

II. 3D SPARSE IMAGING MODEL OF LASAR

A. LINEAR REPRESENTATION MODEL OF LASAR

Assume LASAR works in the downward-looking mode and the geometric model of LASAR is shown in Fig.1, where axis x, axis y, and axis z represents the cross-track(CT), along-track(AT) and range direction respectively. $\boldsymbol{P_A} = \{Q_l = (x_l, y_l, z_l); l \in [1, 2, \ldots, N_A]\}$ is the location set of antenna phase centers(APCs) in the 2D equivalent array synthesized by the moving of linear antenna array (LAA), N_A represents the total number of APCs in the 2D equivalent array.

The LASAR imaging scene is considered as point-targets' scattering model under far-field observing conditions and divided into 3D uniform scattering units. Let $\boldsymbol{P}_S = \{P_m = (x_m, y_m, z_m); m \in \boldsymbol{\Omega}\}$ represent the set of scattering units' locations, where $\boldsymbol{\Omega} = [1, 2, \ldots, M]$ represents the index set of scattering units. Let $\boldsymbol{\alpha} = \mathrm{Vec}[\alpha_m]$ represent the vector of scattering coefficients, where α_m represents the scattering coefficient of P_m, and Vec[.] is the vectorized symbol. Set the LASAR system to transmit the linear frequency modulation signal [35], and the echo signal of P_m after range compression is formulated as:

$$s_r(r, l, m) = \alpha_m \chi_R(r - R_{l,m}) \exp\{-j2kR_{l,m}\} \quad (1)$$

where r represents the range domain, and k represents the wavenumber of LASAR, $R_{l,m} = \| Q_l - P_m \|_2$ is the distance between P_m and Q_l, and $\chi_R(.)$ represents the ambiguity function of range compression. Echo signals of the whole imaging scene are defined as:

$$s_r(r, l) = \sum_{m \in \boldsymbol{\Omega}} s_r(r, l, m) \quad (2)$$

where $s_r(r, l)$ is written as $s_r(r, l) = \{s_r(r_n, l) = \psi(r_n, l)^T \boldsymbol{\alpha}, n = 1, \ldots, N_R\}$, N_R represents the number of sampling points in range domain, and $\psi(r_n, l) = \mathrm{Vec}[\chi_{\mathrm{R}}(r_n - R_{l,m}) \exp(-j2kR_{l,m})]$ represents the vector of delay phase between P_m and Q_l. Then the linear representation model of LASAR is defined as:

$$s_n = \boldsymbol{\Theta}\boldsymbol{\alpha} + n \quad (3)$$

where $s_n = \mathrm{Vec}[s_r(r_n, l)] \in \mathbb{C}^{N_A \times 1}$ represents the echo signal of the nth equidistant plane after range compression, and $\boldsymbol{\Theta} = \mathrm{Vec}[\psi(r_n, l)]^T \in \mathbb{C}^{N_A \times M}$ represents the measurement matrix of s_n, $\boldsymbol{n}$ is the signal noise in s_n. Therefore, the 2D imaging has been translated into getting the optimal value of $\boldsymbol{\alpha}$ through solving (3) by CS algorithms such as OMP, BCS and SBRIM algorithm. SBRIM algorithm is used for imaging in this paper because of its higher imaging quality and stronger ability in suppressing the signal noise than OMP and BCS algorithm. Besides, the basic principle of SBRIM algorithm is introduced in the next subsection.

B. SBRIM ALGORITHM

Set the signal noise $\boldsymbol{n}$ to obey the complex Gaussian random distribution [36]: $f(\boldsymbol{n}) \propto CN(0, \beta \boldsymbol{I})$, where β is the variance of $\boldsymbol{n}$. Then the posterior probability of s_n obeys $f(s_n|\boldsymbol{\alpha}, \beta) \propto CN(\boldsymbol{\Theta}\boldsymbol{\alpha}, \beta \boldsymbol{I})$ according to the linear representation model, where $\boldsymbol{\alpha}$ and s_n represent the scattering coefficients and the echo signal after range compression of nth equidistant plane respectively. Therefore the posterior probability density function (PDF) of s_n is defined as:

$$f(s_n|\boldsymbol{\alpha}, \beta) \propto \frac{1}{(2\pi\beta)^{N_A \backslash 2}} \exp\Big\{ - \frac{\|s_n - \boldsymbol{\Theta}\boldsymbol{\alpha}\|_2^2}{2\beta} \Big\} \quad (4)$$

The scattering units in the SAR image are independently and identically distributed, and their distribution is generally considered as the exponential distribution. Therefore the prior PDF of $\boldsymbol{\alpha}$ is defined as $f(\boldsymbol{\alpha}) \propto \prod_{m=1}^{M} f(\alpha_m) = \prod_{m=1}^{M} \exp(-\lambda_0 |\alpha_m|^p)$, where $\lambda_0 > 0$, and $0 < p \leq 1$. Because β belongs to $[0, \infty)$, the prior PDF of β is defined as $f(\beta) \propto 1$. According to the Bayesian Information Criterion [37], the posterior PDF of $\boldsymbol{\alpha}$ is expressed as:

$$\begin{aligned} f(\boldsymbol{\alpha}|s_n, \beta) \propto & f(s_n|\boldsymbol{\alpha}, \beta) f(\boldsymbol{\alpha}) f(\beta) \\ = & \frac{1}{(2\pi\beta)^{N_A \backslash 2}} \exp\Big\{ - \frac{\|s_n - \boldsymbol{\Theta}\boldsymbol{\alpha}\|_2^2}{2\beta} \Big\} \\ & \times \prod_{m=1}^{M} \exp(-\lambda_0 |\alpha_m|^p) \end{aligned} \quad (5)$$

Calculating the conditional likelihood function of

This article has been accepted for publication in a future issue of this journal, but has not been fully edited. Content may change prior to final publication. Citation information: DOI 10.1109/ACCESS.2019.2959128, IEEE Access

$f(\boldsymbol{\alpha}|s_n,\beta)$, and then we can get:

$$\ln(f(\boldsymbol{\alpha}|s_n,\beta)) = -\frac{N_A \ln 2\pi}{2} - \lambda_0 \sum_{m=1}^{M} |\alpha_m|^p - \left\{ \frac{\|s_n - \boldsymbol{\Theta}\boldsymbol{\alpha}\|_2^2}{2\beta} \right\} - \frac{N_A \ln\beta}{2} \tag{6}$$

$\frac{N_A \ln 2\pi}{2}$ does not influence the optimal estimation of $\boldsymbol{\alpha}$ and β by the Maximum Likelihood (ML) criterion [38]; the conditional likelihood function of $f(\boldsymbol{\alpha}|s_n,\beta)$ is defined as:

$$\begin{aligned} L(\boldsymbol{\alpha},\beta) &= -\left\{ \frac{N_A \ln\beta}{2} + \lambda_0 \sum_{m=1}^{M} |\alpha_m|^p + \frac{\|s_n - \boldsymbol{\Theta}\boldsymbol{\alpha}\|_2^2}{2\beta} \right\} \\ &= -\left\{ \frac{N_A \ln\beta}{2} + \lambda_0 \|\boldsymbol{\alpha}\|_p + \frac{\|s_n - \boldsymbol{\Theta}\boldsymbol{\alpha}\|_2^2}{2\beta} \right\} \end{aligned} \tag{7}$$

The l_p norm of $\boldsymbol{\alpha}$ in (7) can be smoothly approximated by $\|\boldsymbol{\alpha}\|_p \approx \sum_{m=1}^{M} (|\alpha_i|^2 + \eta)^{p\backslash 2}$ [39]. Moreover, the cost function for the optimal estimation of $\boldsymbol{\alpha}$ and β is defined as:

$$J(\boldsymbol{\alpha},\beta) \triangleq N_A \ln\beta + \frac{\|s_n - \boldsymbol{\Theta}\boldsymbol{\alpha}\|_2^2}{2\beta} + \lambda_0 \sum_{m=1}^{M} (|\alpha_i|^2 + \eta)^{p\backslash 2} \tag{8}$$

where η is the smooth factor, and the optimal estimation value of $\boldsymbol{\alpha}$ and β are obtained by solving (9) according to the ML criterion.

$$(\hat{\boldsymbol{\alpha}}, \hat{\beta}) = \arg\lim_{\boldsymbol{\alpha},\beta} J(\boldsymbol{\alpha},\beta) \tag{9}$$

Therefore, we can obtain the 2D imaging results of all equidistant planes through solving (9), and the 3D imaging results by combining every equidistant planar 2D imaging results. Then we summarize the flow diagram of SBRIM algorithm and LASAR 3D imaging as Fig.2.

C. PROBLEMS OF SBRIM ALGORITHM

The computational complexity of SBRIM algorithm in 3D imaging is quantitatively analyzed in this subsection. Define one multiplication and addition as the unit computational complexity: $\vartheta(1)$, and the computational complexity of performing inversion on $\boldsymbol{A} \in \mathbb{C}^{N\times M}$ is equal to $\boldsymbol{A}$ times $\boldsymbol{B} \in \mathbb{C}^{M\times M}$.

The computational complexity of 2D imaging using SBRIM algorithm for the nth equidistant plane is analyzed firstly. According to the flow diagram of SBRIM algorithm shown in Fig.2 (a), the computational complexity of SBRIM algorithm is mainly generated by the multiplication among the vector of scattering coefficients, measurement matrix $\boldsymbol{\Theta}$ and echo signal s_n. For example, when the 2D imaging scene of the nth equidistant plane is divided into $M_0 \times M_0$ scattering units, and the measurement matrix of s_n is $\boldsymbol{\Theta} \in \mathbb{C}^{N_A\times M}$. And the computational complexity of SBRIM algorithm on 2D imaging is $\vartheta(I_S N_A M^2)$, where $M = M_0^2$, N_A represents the total number of APCs in the 2D equivalent array, and I_S represents the number of iterations of SBRIM algorithm. Therefore, the total computational complexity of SBRIM algorithm on LASAR 3D imaging is $\vartheta(N_R I_S N_A M^2)$ according to Fig.2 (b), where N_R represents the number of sampling points in the range direction. Meanwhile, the computational complexity of 3D imaging by MF and OMP algorithm is represented by $\vartheta(N_R N_A M)$ and $\vartheta(K N_R N_A M)$ [40] under the same imaging conditions respectively, where K is the preset sparsity of imaging scene in the OMP algorithm. Therefore, the computational complexity of SBRIM algorithm far exceeds MF and OMP algorithm and we need to study a new sparse imaging algorithm to improve computational efficiency without reducing the imaging quality compared with SBRIM algorithm.

III. FAST SPARSE RECOVERY ALGORITHM BASED ON RESOLUTION APPROXIMATION

To improve the computational efficiency of LASAR 3D imaging, we present a fast sparse recovery algorithm via resolution approximation (FSRARA) in this section, FSRARA mainly consists of the following three steps. Firstly, FSRARA obtains the low-resolution imaging results of the whole imaging scene by SBRIM [28] algorithm quickly. Secondly the low-resolution imaging results are conducted image segmentation by FCM [34] algorithm to extract the possible targets' areas in the whole imaging scene. Finally, we use the possible targets' areas to perform the 3D high-resolution imaging. Moreover, the detailed steps of LASAR 3D imaging by FSRARA are introduced in the following subsections.

A. LOW-RESOLUTION IMAGING

The whole imaging scene is divided into 3D discrete scattering units by a uniform spacing, and the spacing is larger than the traditional array imaging resolution of LASAR. Besides, the spacing is practically set as twice of the traditional array resolution after taking the computational efficiency and imaging quality into overall consideration. Then the 3D low-resolution imaging results $\boldsymbol{\alpha}_0 \in \mathbb{C}^{M_1\times M_1\times N_R}$ of the whole imaging scene are obtained by SBRIM [28] algorithm after I_{s_1} iterations, where N_R represents the total number of sampling points in the range direction.

B. IMAGE SEGMENTATION

After obtaining the low-resolution imaging results $\boldsymbol{\alpha}_0$, $\boldsymbol{\alpha}_0$ is classified into several subclasses through performing image segmentation by the FCM algorithm to obtain the possible targets' areas. To extract the possible targets' areas as completely as possible, the extracting threshold is generated by the subclass imaging results corresponding to the clustering centers with the smallest two amplitudes, and the possible targets' areas are extracted coarsely by the extraction threshold and $\boldsymbol{\alpha}_0$. Then, the imaging scene is re-divided into 3D scattering units by a new uniform spacing smaller than the array imaging resolution. Meanwhile, the possible targets' areas are extracted again according to the preliminary possible targets' areas. In addition, the main steps of extracting the possible targets' areas are introduced as follows:

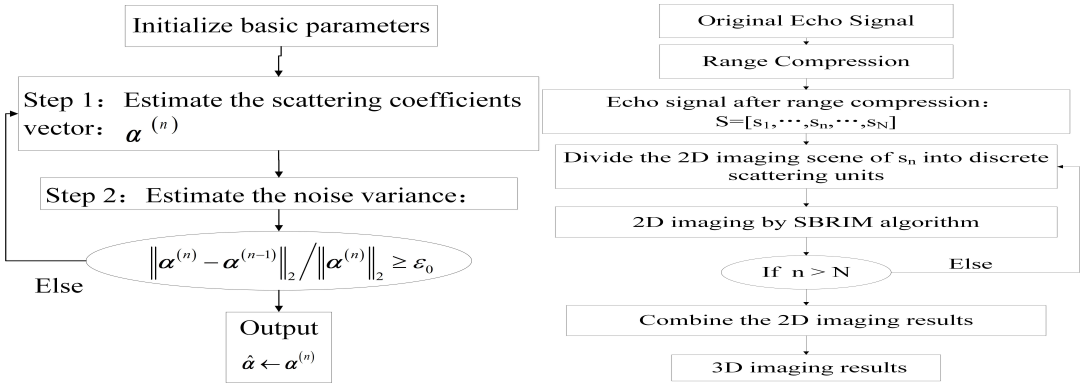

FIGURE 2. **(a) The flow diagram of SBRIM algorithm. (b) The flow diagram of LASAR 3D imaging.**

Step A.1: The nth equidistant planar imaging results in the low-resolution imaging results $\boldsymbol{\alpha}_0$ are extracted and recorded as $\boldsymbol{\alpha}_n = \alpha_n(i,j) = \alpha_0(i,j,n) \in \mathbb{C}^{M_1 \times M_1}, 1 \leq i,j \leq M_1$;

Step A.2: The normalized $\boldsymbol{\alpha}_n$ is obtained and recorded as $\bar{\boldsymbol{\alpha}}_n = \bar{\alpha}_n(i,j)$ by (10):

$$\bar{\alpha}_n(i,j) = \frac{|\alpha_n(i,j)| - \min|\boldsymbol{\alpha}_n|}{\max|\boldsymbol{\alpha}_n| - \min|\boldsymbol{\alpha}_n|} \tag{10}$$

Step A.3: The matrix $\hat{\boldsymbol{\alpha}}_n$ is obtained by conducting the means filtering operation [41] on $\bar{\boldsymbol{\alpha}}_n$;

Step A.4: The Gray scale value of $\hat{\boldsymbol{\alpha}}_n$ is generated and recorded by $\boldsymbol{h}_n = \left\{ h_n(i,j) = \dfrac{|\hat{\alpha}_n(i,j)|}{\max|\hat{\boldsymbol{\alpha}}_n|} \right\} \in \mathbb{C}^{M_1 \times M_1}$ and transformed into $\vec{\boldsymbol{g}}_n = \{g_{n_w} = h_n(i,j); w = (j-1) \times M_1 + i\} \in \mathbb{C}^{M_{Z_1}}$, where $M_{Z_1} = (M_1)^2$ represents the total number of scattering units in the nth equidistant plane.

Step A.5: Initialize the main parameters of image segmentation: the maximum iterations are $T = 100$, the threshold of terminating iterations is $\varepsilon = 10^{-5}$, the fuzzy exponent is $m = 2$, and the number of subclass is $c = 3$, the membership function matrix is initialized by $U^{(0)} = [u_{kn_w}^{(0)}; k = 1, \cdots, c]$, where $u_{kn_w}^{(0)}$ is a random number between 0 and 1 and satisfies $\sum_{k=1}^{c} u_{kn_w}^{(0)} = 1$. The initial value of cluster centers are obtained and recorded as $V^{(0)} = \{v_k^{(0)}; k = 1, \cdots, c\}$ by (11).

$$v_k^{(0)} = \frac{\sum_{w=1}^{M_{Z_1}} (u_{kn_w}^{(0)})^2 g_{n_w}}{\sum_{w=1}^{M_{Z_1}} (u_{kn_w}^{(0)})^2} \tag{11}$$

Step A.6: Update the membership degree function matrix $U^{(t)} = [u_{kn_w}^{(t)}]_{c \times M_{Z_1}}$, where $u_{kn_w}^{(t)}$ represents the extent of g_{n_w} belonging to the subclass imaging results corresponding to $v_k^{(t)}$, $v_k^{(t)}$ represents the value of clustering centers after t iterations, t is the current iteration number.

1): Set $u_{kn_w}^{(t)} = 1$,$u_{pn_w}^{(t)} = 0, p \neq k$, when $d_{kn_w}^{(t)} = 0$;

2): Update $u_{kn_w}^{(t)}$ by (12) when $d_{kn_w}^{(t)} > 0$; where $d_{kn_w}^{(t)} = \|g_{n_w} - v_k^{(t)}\|_2$ is the distance between g_{n_w} and $v_k^{(t)}$.

$$u_{kn_w}^{(t)} = \frac{1}{\sum_{l=1}^{c} (\frac{d_{kn_w}^{(t)}}{d_{ln_w}^{(t)}})^2} \tag{12}$$

Step A.7: Update the cluster center $v_k^{(t+1)}$ by (13);

$$v_k^{(t+1)} = \frac{\sum_{w=1}^{M_{Z_1}} (u_{kn_w}^{(t)})^2 g_{n_w}}{\sum_{w=1}^{M_{Z_1}} (u_{kn_w}^{(t)})^2} \tag{13}$$

Step A.8: Repeat Step A.6 to A.7 if $\|v_k^{(t+1)} - v_k^{(t)}\| > \varepsilon$ or $t < T$; otherwise terminate iteration, and the optimal membership function matrix and clustering centers are obtained and recorded as $U^{(t)} \to U$ and $V^{(t)} \to V$ respectively;

Step A.9: g_{n_w} is divided into the subclass imaging results corresponding to the clustering center with the maximum membership degree function of g_{n_w}. The classification results of $\boldsymbol{h}_n$ are sorted in the ascending order according to the amplitude of v_k and recorded as $\boldsymbol{h}_n = [h_{n_1}, h_{n_2}, h_{n_3}]$, where h_{n_1} and h_{n_3} represent the two subclasses imaging results of nth equidistant plane corresponding to the clustering center with the minimum and maximum amplitude respectively. The extraction threshold for nth equidistant planar imaging results is generated by (14) to extract the possible targets' areas as completely as possible.

$$\rho_0^n = \frac{\max(h_{n_1}) + \min(h_{n_2})}{2} \tag{14}$$

The classification results of the low-resolution imaging results $\boldsymbol{\alpha}_0$ are obtained after traversing all equidistant planar imaging results through Step A.1 to A.9 proposed in this subsection. Besides, the extraction thresholds for $\boldsymbol{\alpha}_0$ are generated and recorded as $\boldsymbol{\rho}_0 = \{\rho_0^n; n = 1, \ldots, N_R\}$ according to the classification results of $\boldsymbol{\alpha}_0$ and (14). The low-resolution imaging results of possible targets' areas are obtained and recorded as $\boldsymbol{\alpha}_s \in \mathbb{C}^{M_1 \times M_1 \times N_R}$ through (15).

$$\begin{cases} \text{If} \quad g_{n_w} \geq \rho_0^n, \alpha_s(i,j,n) = \alpha_n(i,j) \\ \text{If} \quad g_{n_w} < \rho_0^n, \alpha_s(i,j,n) = 0 \end{cases} \tag{15}$$

After obtaining the low-resolution imaging results of pos-

This article has been accepted for publication in a future issue of this journal, but has not been fully edited. Content may change prior to final publication. Citation information: DOI 10.1109/ACCESS.2019.2959128, IEEE Access

sible targets' areas $\boldsymbol{\alpha}_s$, the 2D imaging scene interval of every equidistant plane is re-divided into $M_0 \times M_0$ scattering units by a new uniform spacing, and the spacing is smaller than the array imaging resolution of LASAR, where $M_0 > M_1$. Then the imaging results of possible targets' areas in the re-divided imaging scene $\boldsymbol{\alpha}_f \in \mathbb{C}^{M_0 \times M_0 \times N_R}$ are obtained by performing the linear interpolation operation [42] on $\boldsymbol{\alpha}_s$. Because the linear interpolation operation on $\boldsymbol{\alpha}_s$ leads to the increasing false targets, the possible targets' areas in the re-divided imaging scene are re-extracted through the same method as extracting the possible targets' areas in the low-resolution imaging results. In addition, the classification results of $\boldsymbol{\alpha}_f$ are acquired and recorded as $\boldsymbol{h}_f = \{h_{f_n}; n = 1, \ldots, N_R\} \in \mathbb{C}^{M_0 \times M_0 \times N_R}$; where $h_{f_n} = [h_{f_{n_1}}, h_{f_{n_2}}, h_{f_{n_3}}]$ represents the classification results of the nth equidistant planar imaging results in $\boldsymbol{\alpha}_f$. The extraction thresholds for $\boldsymbol{\alpha}_f$ are generated and recorded as $\boldsymbol{\rho}_f = \{\rho_f^n; n = 1, \ldots, N_R\}$ according to $\boldsymbol{h}_f$ and (14). Moreover, the possible targets' areas in the re-divided imaging scene are extracted and recorded as $\boldsymbol{G} = \{G(x_r, y_r, n); n = 1, \ldots, N_R\}$ by (16).

$$\begin{cases} \text{If} \quad h_{f_n}(i,j) \geq \rho_f^n, (i,j,n) \in G(x_r, y_r, n) \\ \text{If} \quad h_{f_n}(i,j) < \rho_f^n, (i,j,n) \notin G(x_r, y_r, n) \end{cases} \tag{16}$$

where $1 \leq i, j \leq M_0$ and $1 \leq r \leq N_{M_n}$, $G(x_r, y_r, n)$ represents the possible targets' areas in the nth equidistant plane, and N_{M_n} is the number of scattering units in $G(x_r, y_r, n)$.

According to the steps of performing image segmentation, the image segmentation operation on the imaging results does not affect the distribution of the echo signal. However, targets with amplitudes lower than the extraction threshold are lost after extracting the possible targets' areas. Because those targets are also submerged in the background when conducting imaging by CS algorithms such as OMP or SBRIM algorithm directly, the loss of those targets does not affect the image quality of high-resolution imaging. Meanwhile, the false targets and sidelobe interference are suppressed more effectively through extracting the possible targets' areas, and the possible targets' areas are considered as the prior information for high-resolution imaging.

C. HIGH-RESOLUTION IMAGING

After obtaining the possible targets' areas $\boldsymbol{G}$ in III.B, we use the possible targets' areas rather than the whole imaging scene to construct the measurement matrix and perform high-resolution imaging. Hence, the cost function for getting the optimal estimation of $\boldsymbol{\alpha}$ and β has been translated into (17) according to $G(x_r, y_r, n)$ and (7) , where $G(x_r, y_r, n)$ represents the possible targets' areas in the 2D imaging scene of nth equidistant plane, $\boldsymbol{\alpha}$ represents the scattering coefficients of the nth equidistant plane, β represents the variance of the signal noise. Meanwhile, the main process of conducting high-resolution imaging according to the possible targets' areas is introduced in the following content.

$$\begin{aligned} J(\alpha(x_r, y_r, n), \beta) \triangleq\ & N_A \ln\beta \\ & + \frac{\|s_n - \boldsymbol{\Theta}(:, w_r)\alpha(x_r, y_r, n)\|_2^2}{2\beta} \\ & + \lambda \sum_{r=1}^{N_{M_n}} (|\alpha(x_r, y_r, n)|^2 + \eta)^{\frac{p}{2}} \end{aligned} \tag{17}$$

where $1 \leq r \leq N_{M_n}$, N_{M_n} represents the number of scattering units in $G(x_r, y_r, n)$, (x_r, y_r, n) represents the location information of $\alpha(x_r, y_r, n)$, s_n represents the nth equidistant planar echo signal after range compression, $\boldsymbol{\Theta}(:, w_r) = [\Theta(1, w_r), \ldots, \Theta(N_A, w_r); w_r = (y_r - 1)M_0 + x_r]$ is the vector of delay phase for $\alpha(x_r, y_r, n)$, and N_A represents the total number of APC in the 2D equivalent array. Therefore, the high-resolution imaging according to the possible targets' areas has been translated into getting the optimal solution of $\boldsymbol{\alpha}$ and β of the arguments in the function (18), and we use the ML criterion to acquire the optimal value of $\boldsymbol{\alpha}$ and β in the following two steps.

$$(\hat{\boldsymbol{\alpha}}_n, \hat{\boldsymbol{\beta}}_n) = \operatorname{argmin} \lim_{\alpha,\beta} J(\alpha(x_r, y_r, n), \beta) \tag{18}$$

Step B.1: Estimate the scattering coefficients vector $\hat{\boldsymbol{\alpha}}_n^{(t)}$ by noise variance $\hat{\boldsymbol{\beta}}^{(t-1)}$:

Calculate the partial derivative of $J(\hat{\alpha}^{(t-1)}(x_r, y_r, n), \hat{\beta}^{(t-1)})$ for $\hat{\alpha}^{(t-1)}(x_r, y_r, n)$ after $t-1$ iterations, then the partial derivative of $\hat{\alpha}^{(t-1)}(x_r, y_r, n)$ can be formulated as:

$$\begin{aligned} & \frac{\partial J(\hat{\alpha}^{(t-1)}(x_r, y_r, n), \hat{\beta}^{(t-1)})}{\partial \hat{\alpha}^{(t-1)}(x_r, y_r, n)} \\ =& 2\lambda_s^{(t)} \boldsymbol{\Lambda}(\hat{\alpha}^{(t-1)}(x_r, y_r, n)) \times \hat{\alpha}^{(t-1)}(x_r, y_r, n) \\ & + \frac{2\boldsymbol{\Theta}(:, w_r)^H (\boldsymbol{\Theta}(:, w_r)\hat{\alpha}^{(t-1)}(x_r, y_r, n) - s_n)}{\hat{\beta}^{(t-1)}} \end{aligned} \tag{19}$$

where $(x_r, y_r, n) \in G(x_r, y_r, n)$, $w_r = (y_r - 1)M_0 + x_r$, and $\lambda_s^{(t)} = \lambda\hat{\beta}^{(t-1)}$, $\boldsymbol{\Lambda}(\hat{\alpha}^{(t-1)}(x_r, y_r, n)) \in \mathbb{C}^{M_z \times M_z}$ is the diagonal matrix of $\hat{\alpha}^{(t-1)}(x_r, y_r, n)$ and is defined as:

$$\begin{aligned} \boldsymbol{\Lambda}(\hat{\alpha}^{(t-1)}(x_r, y_r, n)) &= \boldsymbol{\Lambda}(w_r, w_r) \\ &= \frac{p}{2}(|\hat{\alpha}^{(t-1)}(x_r, y_r, n)|^2 + \eta)^{\frac{p}{2}-1} \end{aligned} \tag{20}$$

Suppose $\dfrac{\partial J(\hat{\alpha}^{(t-1)}(x_r, y_r, n), \hat{\beta}^{(t-1)})}{\partial \hat{\alpha}^{(t-1)}(x_r, y_r, n)} = 0$, then the estimation value of $\hat{\alpha}^{(t-1)}(x_r, y_r, n)$ satisfies (21).

$$\begin{aligned} & (\boldsymbol{\Theta}(:, w_r)^H \boldsymbol{\Theta}(:, w_r) + \lambda_s^{(t)} \boldsymbol{\Lambda}(\hat{\alpha}^{(t-1)}(x_r, y_r, n))) \\ & \times \hat{\alpha}^{(t-1)}(x_r, y_r, n) = \boldsymbol{\Theta}(:, w_r)^H s_n \end{aligned} \tag{21}$$

It is difficult to directly determine an accurate solution of (21) because of the nonlinear function $\boldsymbol{\Lambda}(\hat{\alpha}^{(t-1)}(x_r, y_r, n))$ of $\hat{\alpha}^{(t-1)}(x_r, y_r, n)$, and efficiently estimated through (22) by the iterative approximation method [43].

$$\begin{aligned} & (\boldsymbol{\Theta}(:, w_r)^H \boldsymbol{\Theta}(:, w_r) + \lambda_s^{(t)} \boldsymbol{\Lambda}(\hat{\alpha}^{(t-1)}(x_r, y_r, n))) \\ & \times \hat{\alpha}^{(t)}(x_r, y_r, n) = \boldsymbol{\Theta}(:, w_r)^H s_n \end{aligned} \tag{22}$$

Therefore, the estimation value of nth equidistant planar scattering coefficients can be obtained after several iterations

and recorded as $\hat{\boldsymbol{\alpha}}_n^{(t)} \in \mathbb{C}^{M_0 \times M_0}$ through (22) and (23).

$$\begin{cases} \text{If}(x_r, y_r, n) \in G(x_r, y_r, n), \hat{\alpha}_n^{(t)}(x_r, y_r) = \hat{\alpha}^{(t)}(x_r, y_r, n) \\ \text{If}(x_r, y_r, n) \notin G(x_r, y_r, n), \hat{\alpha}_n^{(t)}(x_r, y_r) = 0 \end{cases} \tag{23}$$

Step B.2: Estimate the noise variance $\hat{\beta}^{(t)}$ by $\hat{\alpha}^{(t)}(x_r, y_r, n)$:

Calculate the partial derivative of $J(\hat{\alpha}^{(t)}(x_r, y_r, n), \hat{\beta}^{(t-1)})$ for $\hat{\beta}^{(t-1)}$, and the partial derivative can be expressed as:

$$\begin{aligned} &\frac{\partial J(\hat{\alpha}^{(t)}(x_r, y_r, n), \hat{\beta}^{(t-1)})}{\partial \hat{\beta}^{(t-1)}} \\ =&\frac{N_A}{\hat{\beta}^{(t-1)}} - \frac{\|s_n - \boldsymbol{\Theta}(:, w_r)\hat{\alpha}^{(t)}(x_r, y_r, n)\|_2^2}{(\hat{\beta}^{(t-1)})^2} \end{aligned} \tag{24}$$

Suppose $\dfrac{\partial J(\hat{\alpha}^{(t)}(x_r, y_r, n), \hat{\beta}^{(t-1)})}{\partial \hat{\beta}^{(t-1)}} = 0$, then we can obtain the estimation value of $\hat{\beta}^{(t-1)}$ by (25).

$$\hat{\beta}^{(t)} = \frac{\|s_n - \boldsymbol{\Theta}(:, w_r)\hat{\alpha}^{(t)}(x_r, y_r, n)\|_2^2}{N_A} \tag{25}$$

where s_n represents the nth equidistant planar echo signal after range compression, $\boldsymbol{\Theta}(:, w_r)$ is the phase-delay vector for $\hat{\alpha}^{(t)}(x_r, y_r, n)$.

If $\hat{\boldsymbol{\alpha}}_n^{(t)}$ satisfies $\dfrac{\|\hat{\boldsymbol{\alpha}}_n^{(t)} - \hat{\boldsymbol{\alpha}}_n^{(t-1)}\|_2}{\|\hat{\boldsymbol{\alpha}}_n^{(t)}\|_2} < \varepsilon_0$ or $t > I_{S_2}$, then the 2D high-resolution imaging results of the nth equidistant plane are obtained: $\hat{\boldsymbol{\alpha}}_n^{(t)} \rightarrow \hat{\boldsymbol{\alpha}}_n$, where ε_0 represents the iteration termination threshold, I_{S_2} represents the number of iterations in the high-resolution imaging step. Moreover, the 2D high-resolution imaging results of all equidistant planes are obtained after traversing all equidistant planes by Step B.1 to B.2, and the 3D high-resolution imaging results are obtained and recorded as $\hat{\boldsymbol{\alpha}} = \{\hat{\boldsymbol{\alpha}}_n; n = 1, \ldots, N_R\} \in \mathbb{C}^{M_0 \times M_0 \times N_R}$ by combining those 2D imaging results.

In the high-resolution imaging step, we use the possible targets' areas instead of the whole imaging scene to construct the measurement matrix and estimate the scattering coefficients of the imaging scene. Therefore, FSRARA has simplified the high-dimensional matrix-operations on the whole imaging scene with low-dimensional matrix-operations according to the possible targets' areas successfully. Besides, the size of possible targets' areas influences the computational efficiency of the high-resolution imaging step greatly. Because of the sparsity of 3D imaging scene, the percentage of possible targets' areas in the whole imaging scene is very small and FSRARA has improved the computational efficiency efficiently compared with SBRIM algorithm. Meanwhile, through extracting the possible targets' areas and constructing the measurement matrix by the possible targets' areas, the false targets and sidelobe interference have been suppressed more effectively and the measurement matrix indicates the characteristics of targets in the imaging scene better. FSRARA has improved the imaging quality compared with SBRIM algorithm.

D. BASIC STEPS OF LASAR 3D IMAGING BY FSRARA

According to the main steps of the low-resolution imaging, image segmentation and high-resolution imaging, we can summarize the main steps of LASAR 3D imaging by FSRARA in the following contents, meanwhile, the flow chart of FSRARA is shown in Fig. 3.

Step 1: The original echo signals of LASAR are conducted range compression, and echo signals after range compression are recorded as $\boldsymbol{S} = \{s_n; n = 1, \ldots, N_R\}$;

Step 2: Divide the 2D imaging scene interval of every equidistant plane by a uniform spacing into $M_1 \times M_1$ scattering units, the spacing is practically twice of the array imaging resolution of LASAR, and the 3D low-resolution imaging results of the whole imaging scene are obtained and recorded as $\boldsymbol{\alpha}_0 \in \mathbb{C}^{M_1 \times M_1 \times N_R}$ by SBRIM [28] algorithm after I_{s_1} iterations;

Step 3: $\boldsymbol{\alpha}_0$ is classified into several subclasses after performing image segmentation by FCM algorithm, and the extraction thresholds of $\boldsymbol{\alpha}_0$ are generated and recorded as $\boldsymbol{\rho}_0 = \{\rho_0^n; n = 1, \ldots, N_R\}$ by the subclass imaging results corresponding to the clustering centers with the smallest two amplitude. Moreover, the low-resolution imaging results of possible targets' areas are extracted and recorded as $\boldsymbol{\alpha}_s \in \mathbb{C}^{M_1 \times M_1 \times N_R}$ according to the extraction thresholds $\boldsymbol{\rho}_0$ and the low-resolution imaging results $\boldsymbol{\alpha}_0$;

Step 4: Redivide the 2D imaging scene interval of the nth equidistant plane into $M_0 \times M_0$ scattering units by a uniform spacing smaller than the array imaging resolution of LASAR.

Step 5: The imaging results of possible targets' areas in the re-divided imaging scene are obtained by performing the linear interpolation operation on $\boldsymbol{\alpha}_s$ and recorded as $\boldsymbol{\alpha}_f \in \mathbb{C}^{M_0 \times M_0 \times N_R}$, meanwhile, the possible targets' areas are re-extracted and recorded as $\boldsymbol{G} = \{G(x_r, y_r, n); n = 1, \ldots, N_R\} \in \mathbb{C}^{M_0 \times M_0 \times N_R}$ by the same method as Step 3;

Step 6: The 2D high-resolution imaging results of the nth equidistant plane are obtained by performing Step B.1 to B.2 proposed in subsection III.C after I_{s_2} iterations according to $G(x_r, y_r, n)$, and recorded as $\hat{\boldsymbol{\alpha}}_n \in \mathbb{C}^{M_0 \times M_0}$;

Step 7: After traversing the imaging scene of every equidistant plane by Step 4 to Step 6 proposed in this subsection, the 3D imaging results of the whole imaging scene are obtained and recorded as $\hat{\boldsymbol{\alpha}} = \{\hat{\boldsymbol{\alpha}}_n, n = 1, \ldots, N_R\} \in \mathbb{C}^{M_0 \times M_0 \times N_R}$ by combining the 2D imaging results of all equidistant planes.

E. THE COMPUTATIONAL COMPLEXITY OF FSRARA

According to subsection III.C, the computational complexity of LASAR 3D imaging by FSRARA is mainly generated by two parts: the 3D low-resolution imaging of the whole imaging scene, and the 3D high-resolution imaging according to the possible targets' areas.

The computational complexity of 3D low-resolution imaging is $\vartheta(N_R I_{S_1} N_A M_1^4)$ according to the analysis of the computational complexity in subsection II.C; meanwhile, the computational complexity of 3D high-resolution imaging is

This article has been accepted for publication in a future issue of this journal, but has not been fully edited. Content may change prior to final publication. Citation information: DOI 10.1109/ACCESS.2019.2959128, IEEE Access

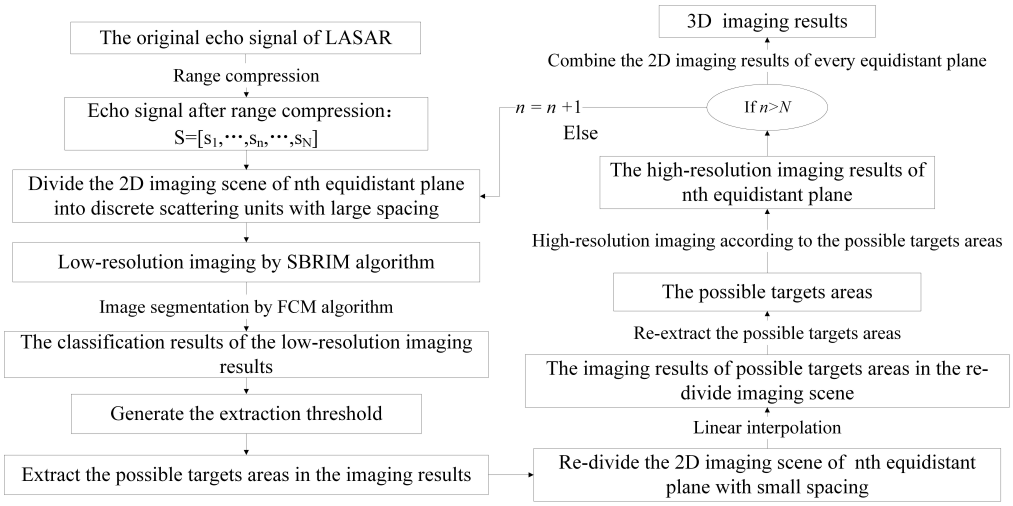

FIGURE 3. The flow chart of LASAR 3D imaging by FSRARA

TABLE I. The computational complexity of SBRIM and FSRARA algorithm on LASAR 3D imaging

Algorithm	Computational complexity
SBRIM algorithm	$\vartheta(N_R I_{S_1} N_A M_0^4)$
FSRARA	$\vartheta(N_R I_{S_1} N_A M_1^4) + \sum_{n=1}^{N_R} \vartheta(I_{S_2} N_A N_{M_n}^2)$

$\sum_{n=1}^{N_R} \vartheta(I_{S_2} N_A N_{M_n}^2 + I_{S_2} N_A N_{M_n}) \approx \sum_{n=1}^{N_R} \vartheta(I_{S_2} N_A N_{M_n}^2)$, which is mainly generated by Step 6 and 7 proposed in subsection III.D. Hence, the total computational complexity of FSRARA on LASAR 3D imaging is $\vartheta(N_R I_{S_1} N_A M_1^4) + \sum_{n=1}^{N_R} \vartheta(I_{S_2} N_A N_{M_n}^2)$, where $I_S = I_{S_1} + I_{S_2}$ represents the total iterations of FSRARA on LASAR 3D imaging, I_{S_1} and I_{S_2} represent the number of iterations in the low-resolution imaging step and high-resolution imaging step respectively, M_1 and M_0 represent the number of scattering units in the low-resolution imaging step and high-resolution imaging step respectively, N_A represents the total number of APCs in the 2D equivalent array, N_{M_n} is the number of scattering units in the possible targets' areas of the nth equidistant planar imaging scene, and N_R represents the amount of sampling points in the range direction. Meanwhile, the computational complexity of SBRIM and FSRARA on LASAR 3D imaging is shown in Table.I.

As seen in Table.I, M_0 and N_{M_n} determines the computational complexity of the SBRIM and FSRARA algorithm on LASAR 3D imaging respectively. However, because of the sparsity of the 3D imaging scene, the percentage of the possible targets' areas in the whole imaging scene is very small. Therefore, FSRARA has reduced the computational complexity significantly compared with SBRIM algorithm.

IV. SIMULATION AND EXPERIMENTAL RESULTS

Both simulation and experimental results are used to certify the effectiveness of FSRARA for LASAR 3D imaging in this section. Meanwhile, the SBRIM algorithm is the main comparison algorithm in this paper because of its high imaging quality. Besides, MF, OMP, IAA, SL0 and BCS algorithms are also used as the comparison algorithm to evaluate the performance of FSRARA better. In order to evaluate the performance of those algorithms in LASAR 3D imaging quantitatively, the running time speed-up (RTS), the normalized mean square error (NMSE), targets background contrast (TBR) [44], and image entropy (ENT) [45] are used in this section. The **RTS** is used to compare the computational efficiency of different algorithms. Meanwhile, **NMSE**, **TBR**, and **ENT** are used to evaluate the imaging quality.

RTS is defined by $\mathrm{RTS} = T_{CS}/T_{RA}$, where T_{CS} represents the running time of LASAR imaging by one algorithm, and T_{RA} represents the running time of the other algorithm. The RTS illustrates the comparison of computational efficiency between two algorithms.

NMSE is defined by $\mathrm{NMSE} = \dfrac{\|\hat{\boldsymbol{\alpha}} - \boldsymbol{\alpha}\|_2}{\|\boldsymbol{\alpha}\|_2}$, where $\boldsymbol{\alpha}$ is the original scattering coefficients of the imaging scene, and $\hat{\boldsymbol{\alpha}}$ is the estimation value of $\boldsymbol{\alpha}$. The smaller NMSE illustrates that the estimation results are more approximate to the original scattering coefficients.

ENT is defined by $\mathrm{ENT} = \sum_{g(i)} p(i) \log p(i)$, where $p(i)$ represents the percentage of the pixel with the Gray value i, and g represents the total number of Gray values in imaging results. ENT is used to characterize the texture of the image; the image is sharper with smaller ENT.

TBR is defined by $\mathrm{TBR} = 20 \log \left\{ \dfrac{N_T}{N_B} \dfrac{\sum_{i \in T}(|\hat{\alpha}_i|)}{\sum_{j \in B}(|\hat{\alpha}_j|)} \right\}$, where T and B are obtained by (26) and represent the index set of targets and background in the imaging results respectively, N_T and N_B represents the number of elements in T and B respectively. The bigger TBR proves that targets are easier to be identified from the imaging results.

$$\begin{cases} \text{If} |\hat{\alpha}_n(x,y)| \geq max(|\hat{\boldsymbol{\alpha}}|) * \gamma, (x,y,n) \in T \\ \text{If} |\hat{\alpha}_n(x,y)| < max(|\hat{\boldsymbol{\alpha}}|) * \gamma, (x,y,n) \in B \end{cases} \quad (26)$$

This article has been accepted for publication in a future issue of this journal, but has not been fully edited. Content may change prior to final publication. Citation information: DOI 10.1109/ACCESS.2019.2959128, IEEE Access

TABLE II. The basic parameters of point-targets simulation

Parameters	value
Center frequency /GHz	30
Size of 2D array /m	4×4
Signal bandwidth /GHz	0.8
Number of elements in AT direction	40
Platform height /m	1000
Number of elements in CT direction	40

where $1 \leq x, y \leq M_0$, $\hat{\boldsymbol{\alpha}} \in \mathbb{C}^{M_0 \times M_0 \times N_R}$ represents the 3D imaging results, M_0 represents the number of scattering units, N_R represents the number of sampling points in the range direction, and γ represents the judgment threshold between the targets and background in $\hat{\boldsymbol{\alpha}}$.

A. SIMULATION RESULTS

B. SIMULATIONS OF POINT-TARGETS

In this subsection, the point-targets simulations for one 2D equidistant plane are conducted to verify the effectiveness of FSRARA for high-resolution imaging. The main parameters and the original scene of the point-targets simulation are shown in Table.II and Fig.5 (a) respectively, and the 2D imaging scene is divided into 101×101 scattering units along the CT and AT direction. Moreover, imaging results of MF, OMP, IAA, SL0, BCS, SBRIM, and FSRARA algorithms are shown in Fig.4. As seen in Fig.4, MF algorithm suffers from severe sidelobe interference and low imaging resolution. Meanwhile, all CS algorithms used in this paper have a stronger ability to eliminate sidelobe interference and obtain higher imaging resolution compared with MF algorithm.

To evaluate the performance of FSRARA better and more detailed, we conduct point-targets simulations under different imaging conditions such as **the sampling rate, signal to noise ratio (SNR)** [46] **and amount of scattering units**. Meanwhile, 200 Monte Carlo trials of FSRARA and OMP algorithm are conducted to evaluate the performance better; however, the Monte Carlo trials of another four algorithms are set as 50 times because of the huge computational complexity. The point-targets simulations under different sampling rate of echo signal are conducted firstly. Besides, the sampling rate is calculated by **Sampling Rate** $= \dfrac{N}{N_A}$ and belongs to $5\% \sim 100\%$, where N_A represents the total number of APCs in the 2D equivalent array and N represents the number of APCs used for LASAR 3D imaging, and the evaluation results under different sampling rates with 101×101 scattering units are shown in Fig.5.

As seen in Fig.5, the NMSE and ENT of all algorithms increase with the decreasing sampling rate because of the increasing sparsity of echo signal; while, TBR decreases with the decreasing sampling rate. As seen in Fig.5 (a)$\sim$(c), the NMSE of the IAA algorithm under different sampling rates is greater than 0.4 and larger than that of other algorithms. Meanwhile, the NMSE of OMP and SL0 algorithm is larger than 0.3 when the sampling rate is smaller than 30%.

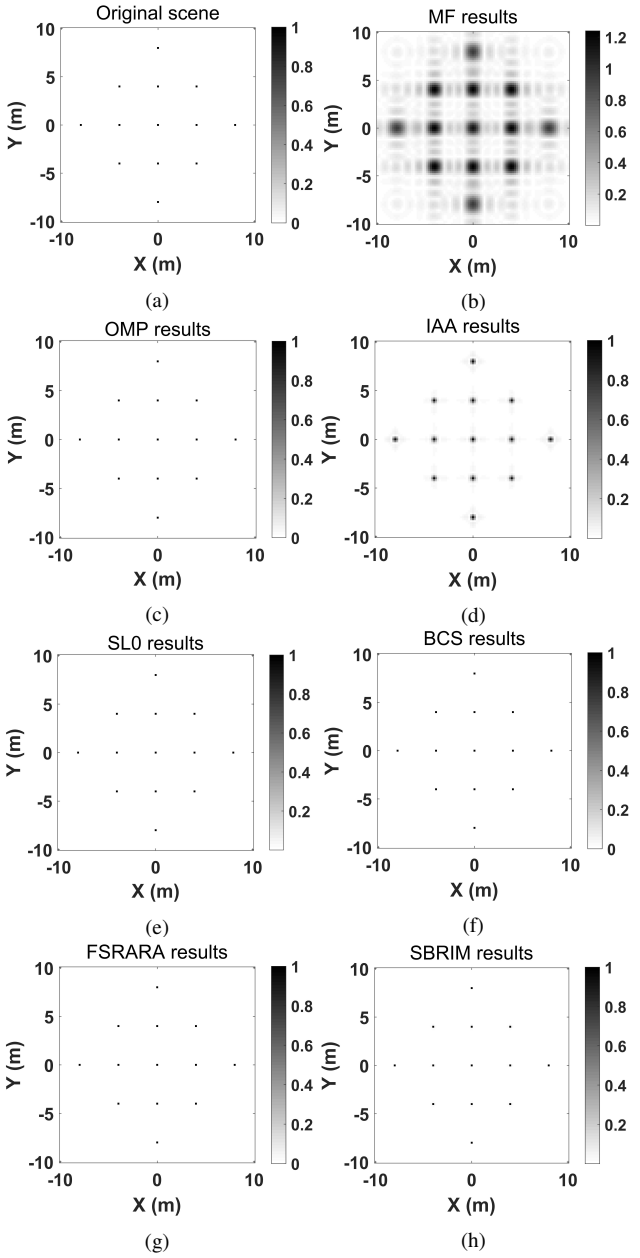

FIGURE 4. (a) Original scene. (b) Imaging results of MF algorithm. (c) Imaging results of OMP algorithm.(d) Imaging results of IAA algorithm. (e) Imaging results of SL0 algorithm. (f) Imaging results of BCS algorithm.(g) Imaging results of SBRIM algorithm. (h) Imaging results of FSRARA algorithm.

Therefore, OMP algorithm cannot achieve high-resolution imaging under sampling rate lower than 30% because of the limited preset sparsity of the imaging scene. Meanwhile, SL0 algorithm cannot estimate the scattering coefficients accurately under sampling rate smaller than 30% because of the fixed iterative step length of the Steepest descent method in SL0 algorithm. Moreover, the NMSE of BCS algorithm is second only to the IAA algorithm and larger than 0.3 when the sampling rate is less than 50%. Because several parameters such as the noise variance or iterative termination threshold are needed to be preset when the BCS algorithm

This article has been accepted for publication in a future issue of this journal, but has not been fully edited. Content may change prior to final publication. Citation information: DOI 10.1109/ACCESS.2019.2959128, IEEE Access

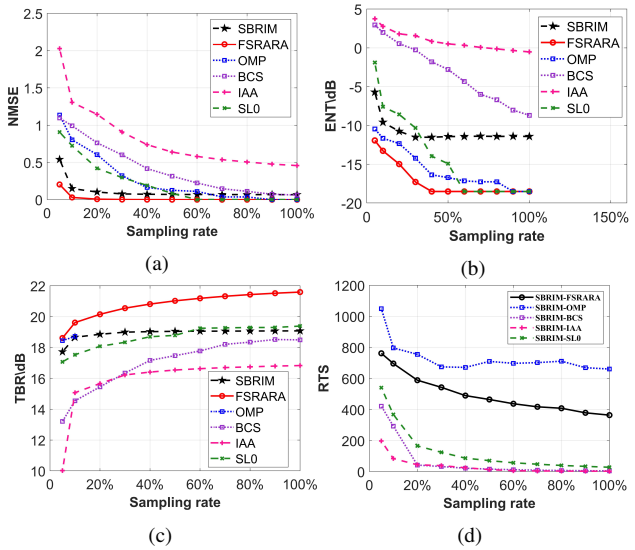

FIGURE 5. Evaluation results under different sampling rates. (a)NMSE. (b) TBR.(c) ENT. (d)RTS.

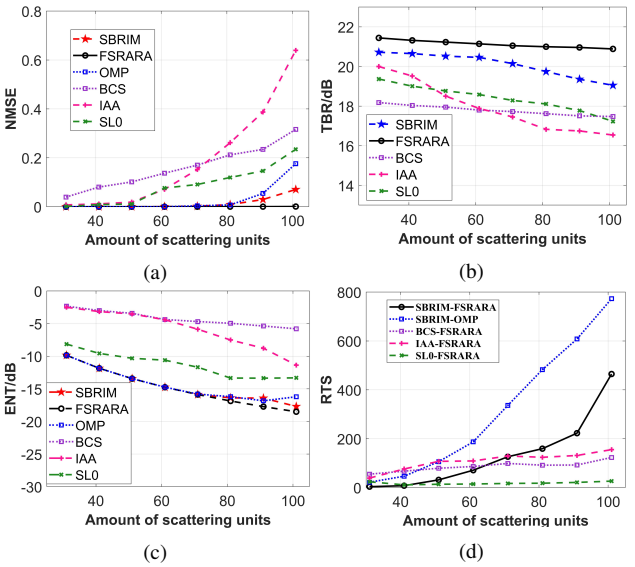

FIGURE 6. Evaluation results under different amount of scattering units. (a)NMSE. (b) TBR.(c) ENT.(d) RTS.

is used for imaging and the preset parameters cannot satisfy the requirement of the high-resolution imaging under all sampling rates entirely, which makes BCS algorithm fail to obtain high-quality imaging results under the sampling rate lower than 50%.

Compared with the BCS algorithm, SBRIM and FSRARA algorithm obtain imaging results with higher imaging quality by assuming the imaging scene obey the exponential distribution and reducing the preset parameters. They suppress the influence of echo signal's increasing sparsity better and obtain imaging results with smaller NMSE compared with OMP and SL0 algorithm under sampling rate smaller than 60%. However, in the high-resolution imaging step, the measurement matrix is constructed by the possible targets' areas and represents the targets' characteristics in the imaging scene better. In conclusion, through conducting high-resolution imaging by the possible targets' areas, FSRARA obtains imaging results with higher TBR, smaller NMSE, and ENT compared with SBRIM algorithm. Besides, the execution time of FSRARA is smaller than SBRIM, BCS, IAA and SL0 algorithm, albeit larger than MF and OMP algorithm. The computational efficiency of SBRIM algorithm has been improved about 300 times by FSRARA, which encounters our goal of proposing a new sparse 3D LASAR imaging method. And the improvement of computational efficiency increases with the increasing sparsity influenced by the decreasing sampling rate. Therefore, FSRARA obtains imaging results with higher imaging quality and greater computational efficiency compared with SBRIM algorithm, and has better performance under higher sparsity.

To evaluate the performance of FSRARA under different imaging resolution, point-targets simulations under different amount of scattering units are conducted secondly. The numbers of scattering units change from 31×31 to 101×101 along CT and AT direction, and the evaluation results under different amount of scattering units with sampling rate 50% are shown in Fig.6.

As seen in Fig.6 (a)$\sim$ (c), NMSE of those algorithms above increase because of the increasing imaging resolution as the growth of scattering units. The covariance matrix in the IAA algorithm reaches its singular value more quickly as the increasing imaging resolution, which limits the number of iterations in the IAA algorithm. Meanwhile, the high-dimensional matrix-operations limit the number of iterations further, the limited iterations make the imaging results of the IAA algorithm suffer from false targets or sidelobe interference seriously. The NMSE of IAA algorithm is larger than 0.4 when the number of scattering units is larger than 81×81. Moreover, the difficulty of presetting the parameters of the BCS algorithm accurately increases as the increasing imaging resolution, which makes the influence of false targets or sidelobe interference increase gradually. Therefore, BCS algorithm has obtained imaging results with higher NMSE and ENT, and smaller TBR compared with SL0, SBRIM, and FSRARA algorithm. Meanwhile, the NMSE of the OMP algorithm increases as the increasing imaging resolution because of the limitation of preset sparsity. When the number of scattering units is larger than 71×71, OMP algorithm obtains imaging results with larger NMSE compared with SBRIM and FSRARA algorithm.

Because SBRIM algorithm has reduced the preset parameters successfully compared with BCS algorithm, SBRIM algorithm can achieve high-quality imaging even under high imaging resolution. Meanwhile, the measurement matrix of FSRARA indicates the targets' characteristics in the imaging scene better. FSRARA eliminates the sidelobe interference and false targets better and obtains imaging results with larger TBR, and smaller ENT and NMSE compared with SBRIM algorithm. As seen in Fig.6(d), because of the decreasing percentage of possible targets' areas in the imaging scene as the increasing scattering units, the RTS between

This article has been accepted for publication in a future issue of this journal, but has not been fully edited. Content may change prior to final publication. Citation information: DOI 10.1109/ACCESS.2019.2959128, IEEE Access

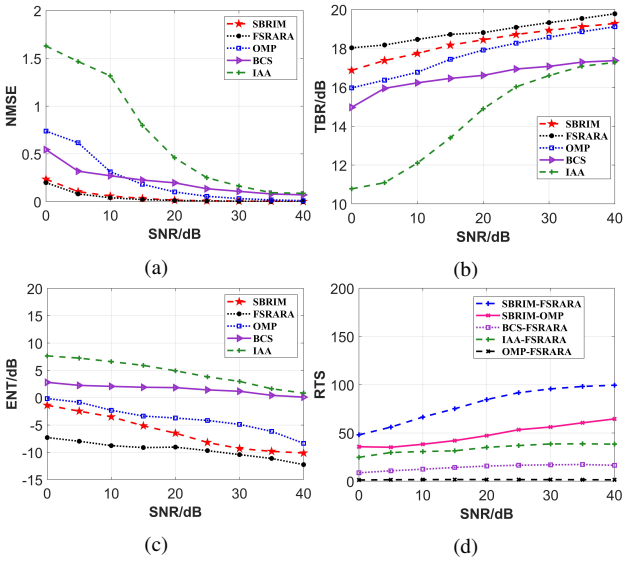

FIGURE 7. Evaluation results under different SNR. (a)NMSE. (b) TBR.(c) ENT.(d) RTS.

FSRARA and other algorithms increase gradually. Therefore, FSRARA has better performance in improving computational efficiency when the imaging resolution is higher. Meanwhile, the RTS between SBRIM and FSRARA is bigger than 50 when the number of scattering units is larger than 61×61. The execution time of FSRARA is larger than the OMP algorithm and smaller than another four algorithms.

To evaluate the ability of FSRARA in eliminating the influence of signal noise on high-quality imaging, point-targets simulations under different SNR [46] are conducted finally. Meanwhile, because SL0 algorithm cannot obtain high-quality imaging results under low SNR, SL0 algorithm is not used as the comparison algorithm in point-targets simulation under different SNR. The SNR of the echo signal belongs to $0 \sim 40$, and the evaluation results under different SNR with 81×81 scattering units and 100% sampling rate are shown in Fig.7.

As seen in Fig.7 (a)$\sim$(c), both NMSE and ENT decrease as the growth of SNR because of the decreasing false targets and sidelobe interference; however, TBR increases with the growth of SNR. The NMSE of the IAA algorithm is the largest and greater than 0.5 when the SNR is smaller than 20 dB because of the limited iterations caused by the huge computational complexity. Moreover, NMSE of the OMP algorithm increases as the decreasing SNR because of the limited preset sparsity of the imaging scene and is larger than SBRIM and FSRARA, and bigger than 0.3 under SNR smaller than 10. Because the scattering coefficients of the imaging scene do not obey the Gaussian distribution and the preset parameters cannot satisfy the requirement of high-resolution imaging under low SNR, the imaging results of the BCS algorithm suffers from false targets and sidelobe interference seriously under low SNR.

Different from BCS algorithm, both SBRIM and FSRARA algorithm assume the imaging scene obey the exponential prior distribution and only preset λ_0 and p to achieve high-resolution imaging. They have a stronger ability to suppress the signal noise under low SNR compared with OMP, IAA, and BCS algorithm. Meanwhile, through extracting the possible targets' areas and performing high-resolution imaging by the possible targets' areas, FSRARA has eliminated the false targets or sidelobe interference better and obtained imaging results with smaller NMSE, ENT, and bigger TBR compared with SBRIM algorithm. As seen in Fig.7(d), the decreasing false targets and sidelobe interference with the growing of SNR reduces the size of the possible targets' areas and the computational complexity of FSRARA. However, the computational efficiency of the SBRIM, BCS, and IAA algorithms is not affected by the SNR, which makes the RTS between SBRIM, BCS, and IAA and FSRARA algorithms increase as the increasing SNR. And the execution time of FSRARA is between MF and OMP algorithm, and RTS between SBRIM and FSRARA is bigger than 50.

According to the simulations in this subsection, the covariance matrix and the high-dimensional matrix-operations have limited the number of iterations of IAA algorithm, the limited iterations make the imaging results of IAA algorithm are affected by the sidelobe interference or false targets seriously. Meanwhile, SL0 algorithm cannot obtain high-quality imaging results under low SNR, and this disadvantage has constrained the application of SL0 algorithm. Moreover, because of the preset sparsity of the imaging scene, OMP algorithm cannot suppress the influence of false targets or sidelobe interference effectively as the increasing imaging resolution or sparsity or decreasing SNR. Meanwhile, the preset parameters in the BCS algorithm cannot satisfy the requirement of high-quality imaging entirely, which makes the imaging results of BCS algorithm suffer from sidelobe interference or false targets.

Both SBRIM and FSRARA algorithm have eliminated the sidelobe interference or false targets better and obtained imaging results with higher quality compared with BCS algorithm by reducing the preset parameters. However, the measurement matrix indicates the characteristics of targets in the imaging scene better, and FSRARA has eliminated the influence of signal noise better than SBRIM algorithm. Meanwhile, FSRARA has reduced the dimensions of the measurement matrix and simplified the high-dimensional matrix-operations into the calculation of corresponding elements in the possible targets' areas successfully. Therefore, FSRARA improves the computational efficiency significantly and obtains imaging results with higher quality compared with SBRIM algorithm. The computational efficiency of FSRARA is mostly lower than the OMP and MF algorithm and higher than BCS, IAA, SL0, and SBRIM algorithm. Moreover, FSRARA has better performance in improving computational efficiency when the sparsity of the imaging scene is stronger, or the imaging resolution is higher.

C. SIMULATIONS OF COMPLEX TARGETS

The simulations of complex targets are conducted to analyze the performance of FSRARA for LASAR 3D imaging further

This article has been accepted for publication in a future issue of this journal, but has not been fully edited. Content may change prior to final publication. Citation information: DOI 10.1109/ACCESS.2019.2959128, IEEE Access

TABLE III. The basic parameters of 3D simulation simulation

Parameters	value
Center frequency /GHz	37.5
Length of array in AT direction /m	3
Signal bandwidth /GHz	0.8
Length of array in CT direction /m	3
Platform height /m	1000
Sampling points in range domain	512
Number of elements in AT direction	64
Number of elements in CT direction	64
Sampling frequency /GHz	1.25
Pulse repetition interval /μs	2

in this subsection. The main parameters of complex targets simulation are shown in Table.III, meanwhile, the original imaging scene and the 3D imaging results of complex targets are shown in Fig.8. As seen in Fig.8, OMP, BCS, SBRIM, and FSRARA algorithm achieve 3D high-quality imaging for complex targets and have a stronger ability in suppressing sidelobe interference than MF algorithm. Meanwhile, the imaging results of SL0 algorithm suffer from the sidelobe interference seriously because of the signal noise in the echo signal. Moreover, the high-dimensional matrix-operations make the computational efficiency of 3D imaging by IAA algorithm unacceptable. For example, the running time of 3D imaging by IAA algorithm is about 102 hours when the 2D imaging scene of every equidistant plane is divided into 41×41 scattering units, and the iterations of IAA algorithm are 3 times, and the computer's primary hardware devices are listed as follows: Core I7 8700K, 64GB RAM, and the NVIDIA GeForce GTX 1080Ti. Therefore, both IAA and SL0 algorithms are not used as the comparison algorithms in this subsection. Meanwhile, because the original scattering coefficients of 3D imaging scene are hardly calculated, **TBR, ENT and RTS** are used to evaluate the performance of algorithms above in this subsection. Fig.9 shows the evaluation results under **different amount of scattering units with the sampling rate** 100% **and SNR 20 dB** . The 2D imaging scene is divided into 51×51 to 101×101 scattering units.

As seen in Fig.8, BCS, SBRIM, and FSRARA algorithm can achieve 3D high-quality imaging without the preset sparsity comparing to the OMP algorithm. However, because the preset parameters in BCS algorithm cannot meet the requirement of 3D high-quality imaging totally, BCS algorithm has lost some targets' information and cannot obtain 3D high-quality imaging results. Meanwhile, both SBRIM and FSRARA has obtained imaging results with higher quality by reducing the preset parameters compared with BCS algorithm. And as seen in Fig.9, the computational complexity of BCS algorithm is higher than SBRIM and FSRARA algorithm. Meanwhile, FSRARA has obtained imaging results with bigger TBR and smaller ENT compared with OMP and SBRIM algorithm, and the RTS between SBRIM and FSRARA increases as the growth of scattering units and is bigger than 50 when the amount of scattering units is larger than 61×61. Meanwhile, the execution time of FSRARA is between MF and OMP algorithm. Therefore, FSRARA improves the computational efficiency of SBRIM algorithm significantly; and improves the imaging quality for LASAR 3D imaging compared with SBRIM algorithm by conducting 3D high-resolution imaging by the possible targets' areas.

D. EXPERIMENTAL RESULTS

In order to verify the effectiveness of FSRARA for the experimental data, the experimental data obtained by the X-band ground equivalent LASAR (X-GDLASAR) experimental system is used for 3D imaging in this subsection. The X-GDLASAR system obtains a high range resolution through transmitting the stepped frequency signal with wide bandwidth by vector network analyzer. Meanwhile, the main parameters of X-GDLASAR system are shown as follows: the center frequency of the X-GDLASAR system is 10 GHz, the signal bandwidth is 2 GHz, the size of the 2D equivalent array is 1.5×1.3 m. The geometric model of two balls experiment is shown in Fig.10 (b), there are two copper balls in the imaging scene, and the distance between ball one and the X-GDLASAR system is 5 m. Firstly, the possible targets' echo signals are extracted to avoid useless computation and decrease the influence of false targets according to the locations of two balls. Meanwhile, MF, OMP, SL0, IAA, BCS, and SBRIM algorithm are used for high-quality imaging and considered as the comparison algorithms to evaluate the performance of FSRARA in 3D imaging of the experimental data better, and the imaging results of those algorithms are shown in Fig.11.

As seen in Fig.11, MF algorithm has obtained imaging results with severe sidelobe interference, and SL0 algorithm cannot obtain high-quality imaging results because of the inevitable signal noise in the echo signal of the experimental data, then SL0 algorithm is not used as the comparison algorithm to evaluate the performance of FSRARA in the 3D imaging of experimental data. Meanwhile, we have obtained imaging results of other 5 CS algorithms used in this paper **under different amount of scattering units** to evaluate the performance of FSRARA for the experimental data better, and the 2D imaging scene interval of every equidistant plane is divided into 31×31 to 101×101 scattering units. Fig.12 shows the evaluation results under different amount of scattering units with the **sampling rate** 100%.

As seen in Fig.11, the imaging results of the OMP algorithm has lost some targets' information and suffered from sidelobe interference because of the limited preset sparsity of imaging scene. According to Fig.11 (c) and Fig.12 (b), the high-dimensional matrix-operations and the huge echo signal makes the computational complexity of IAA algorithm very huge. For example, the running time of 3D imaging by IAA algorithm is more than 20 hours when the imaging scene of every 2D equidistant plane is divided into 61×61 scattering units. Besides, the iterations of the IAA algorithm are set to 3 times to avoid the covariance matrix reaching its singular

This article has been accepted for publication in a future issue of this journal, but has not been fully edited. Content may change prior to final publication. Citation information: DOI 10.1109/ACCESS.2019.2959128, IEEE Access

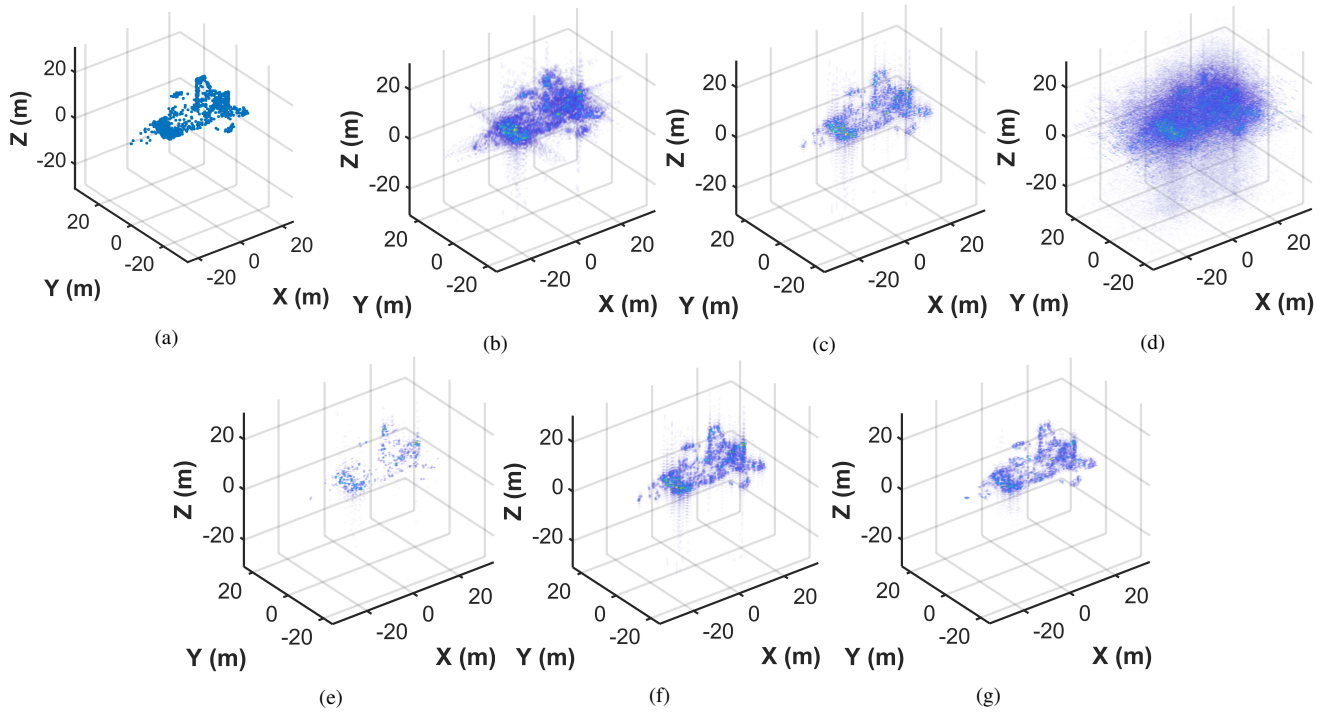

FIGURE 8. The original scene and imaging results of complex targets. (a) Original scene. (b) Imaging results of MF algorithm. (c) Imaging results of OMP algorithm. (d) Imaging results of SL0 algorithm. (e) Imaging results of BCS algorithm. (f) Imaging results of SBRIM algorithm. (g) Imaging results of FSRARA algorithm.

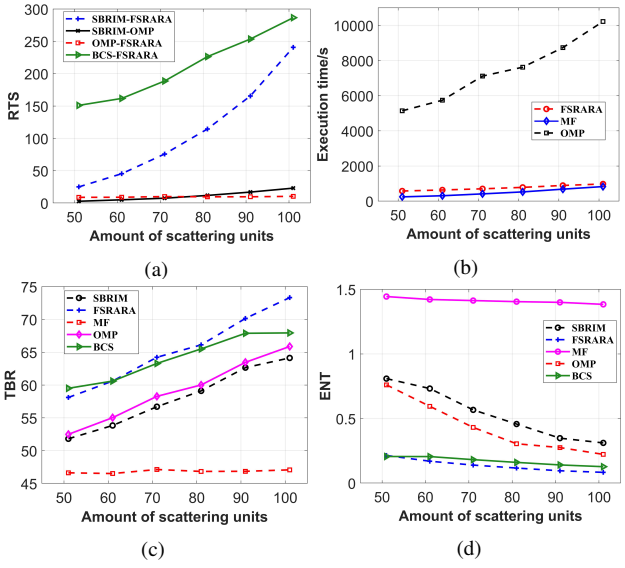

FIGURE 9. Evaluation results of complex targets simulations under different scattering units. (a)RTS. (b) Execution time. (c) TBR.(d) ENT

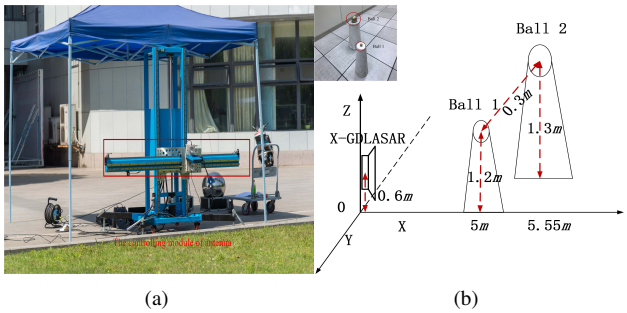

FIGURE 10. (a)The X-GDLASAR system. (b) The geometric model of two balls experiment.

value. Meanwhile, because of the inevitable signal noise in the echo signal and the limited iterations, the imaging results of IAA algorithm are influenced by the sidelobe interference and false targets terribly.

As seen in Fig.11 and 12, because the preset parameters in BCS algorithm hardly meet the requirements of all equidistant plane high-quality imaging for the experimental data, the imaging results of the BCS algorithm are terribly affected by the sidelobe interference. Moreover, the execution time of 3D imaging by IAA and BCS algorithm is higher than SBRIM algorithm. Besides, both SBRIM and FSRARA algorithm have eliminated the sidelobe interference better than BCS algorithm by reducing the preset parameters, and they have obtained imaging results with higher imaging quality compared with IAA and BCS algorithm. FSRARA has obtained imaging results with higher TBR and smaller ENT compared with other four algorithms. Meanwhile, the execution time of FSRARA is between MF and OMP algorithm. RTS between SBRIM and FSRARA increases as the growth of scattering units and is bigger than 50 when the amount of scattering units is larger than 61×61. There exist false targets in the extracted echo signal's region after extracting the echo signal according to the targets' position, all CS algorithms used for LASAR 3D imaging are influenced by the false targets' in-

This article has been accepted for publication in a future issue of this journal, but has not been fully edited. Content may change prior to final publication. Citation information: DOI 10.1109/ACCESS.2019.2959128, IEEE Access

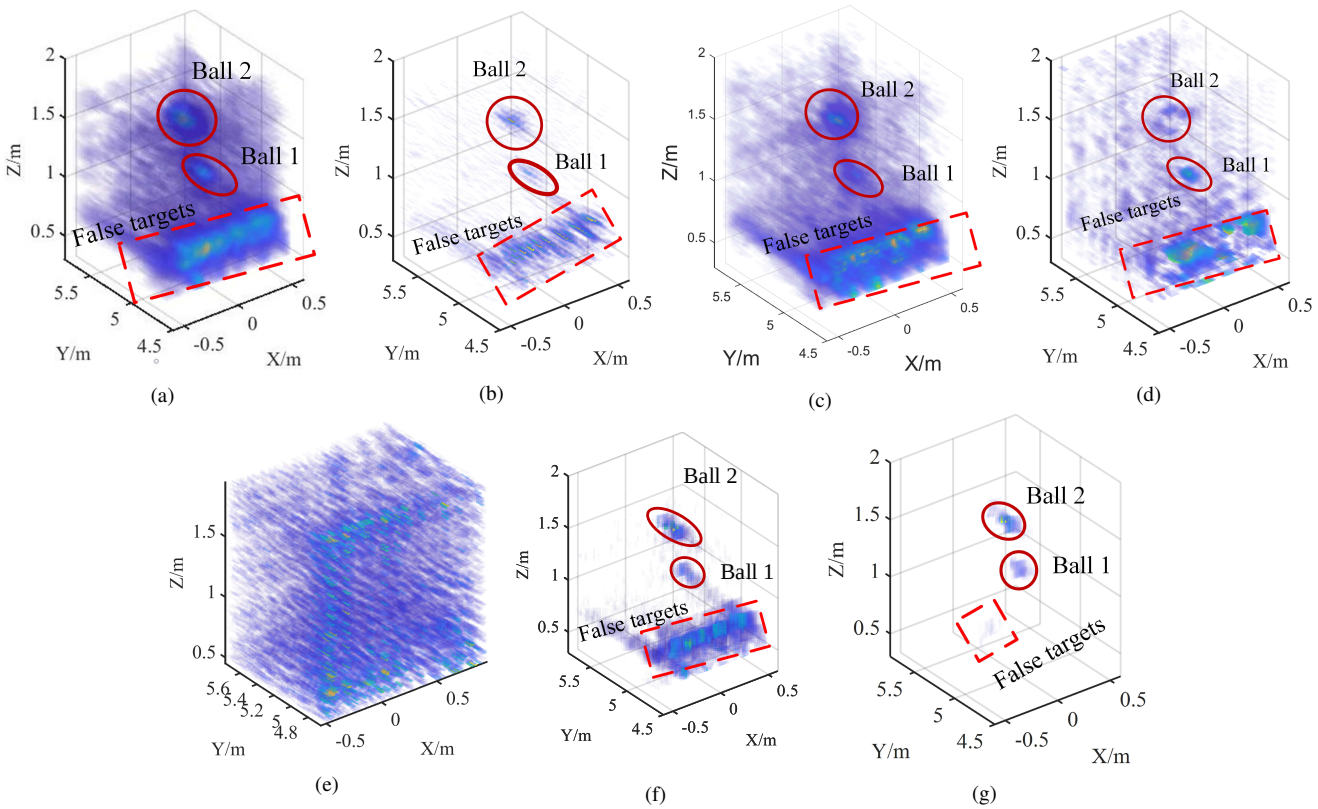

FIGURE 11. **Imaging results of two balls experiment. (a)MF algorithm. (b) OMP algorithm.(c) IAA algorithm. (d) BCS algorithm. (e) SL0 algorithm. (f) SBRIM algorithm. (g) FSRARA**

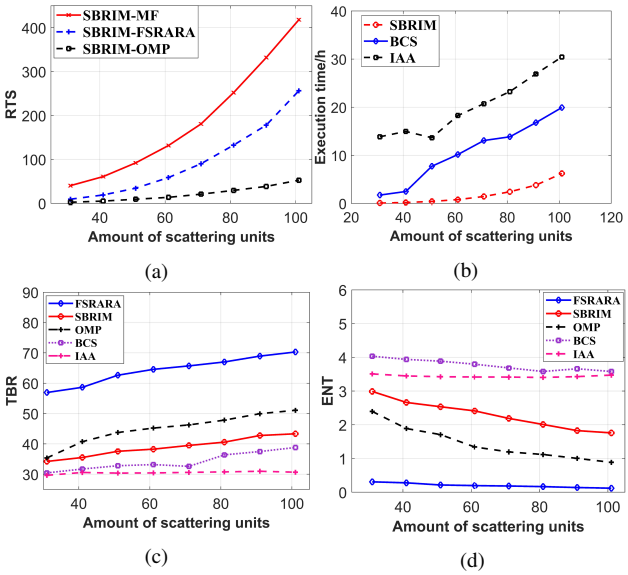

FIGURE 12. **Evaluation results of two balls experiment under different scattering units. (a)RTS. (b) Execution time. (c) TBR. (d) ENT**

terference, except the FSRARA. Through extracting the possible targets' areas in the imaging scene and conducting 3D imaging according to the possible targets' areas, FSRARA eliminates the false targets in the imaging scene better. To summarize, FSRARA can improve the imaging quality and computational efficiency for LASAR 3D imaging compared with SBRIM algorithm according to the experimental results in this subsection.

V. CONCLUSION

In this paper, a novel algorithm named FSRARA is proposed to improve the computational efficiency of CS algorithms. FSRARA has replaced the high-dimensional matrix-operations on the whole imaging scene with the low-dimensional matrix-operations on the possible targets' areas, additionally, the size of the possible targets' areas is far smaller than the whole 3D imaging scene because of the sparsity of the 3D imaging scene. Both simulation and experimental results demonstrated that the computational efficiency of FSRARA has been improved by hundreds of times at most compared with SBRIM algorithm. The computational efficiency of FSRARA is lower than MF algorithm and higher than SL0, IAA, and BCS algorithms. Meanwhile, the computational efficiency of FSRARA is lower than the OMP algorithm except for the case of large preset sparsity in the OMP algorithm. Besides, the false targets and sidelobe interference has been suppressed effectively by just using the possible targets' areas to construct the measurement matrix, and the measurement matrix indicates the characteristics of targets in the imaging scene better. FSRARA obtained 3D imaging results with higher imaging quality compared with OMP, SL0, IAA, BCS, and SBRIM algorithm. Simulation and experimental results have confirmed our conclusions well.

REFERENCES

[1] M. L. Bryant and L. L. Gostin and M. Soumekh, "3-D E-CSAR imaging of a T-72 tank and synthesis of its SAR reconstructions," IEEE Transactions on Aerospace and Electronic Systems, vol. 39, no. 1, pp. 211–227, Jan. 2003, 10.1109/TAES.2003.1188905.

[2] A. Budillon and G. Schirinzi, "GLRT Based on Support Estimation for Multiple Scatterers Detection in SAR Tomography," IEEE Journal of Selected Topics in Applied Earth Observations and Remote Sensing, vol. 9, no. 3, pp. 1086–1094, Mar. 2016, 10.1109/JSTARS.2015.2494376.

[3] S. Jun and Z. Xiaoling and Y. Jianyu and W. Chen, "APC Trajectory Design for "One-Active" Linear-Array three-dimensionalal Imaging SAR," IEEE Transactions on Geoscience and Remote Sensing, vol. 48, no. 3, pp. 1470–1486, Mar. 2010, 10.1109/TGRS.2009.2031430.

[4] V. M. Patel and G. R. Easley and D. M. Healy, Jr. and R. Chellappa, "Compressed Synthetic Aperture Radar," IEEE Journal of Selected Topics in Signal Processing, vol. 4, no. 2, pp. 244–254, Feb. 2010, 10.1109/JSTSP.2009.2039181.

[5] Y. Tsaig and D. L.Donoho, "Extensions of compressed sensing," Signal Processing, vol. 86, no. 3, pp. 549–571, Mar. 2006, 10.1016/j.sigpro.2005.05.029.

[6] D. L. Donoho, "Compressed Sensing," IEEE Transactions on Information Theory, vol. 52, no. 4, pp. 1289–1306, May. 2006, 10.1109/TIT.2006.871582.

[7] E . J. Candes and T. Tao, "Near-Optimal Signal Recovery From Random Projections: Universal Encoding Strategies," IEEE Transactions on Information Theory, vol. 52, no. 12, pp. 5406–5425, Nov. 2006, 10.1109/TIT.2006.885507.

[8] K. Liao and X. Zhang and J. Shi, "Plane-Wave Synthesis and RCS Extraction via 3-D Linear Array SAR," IEEE Antennas and Wireless Propagation Letters, vol. 14, pp. 994–997, Dec. 2015, 10.1109/LAWP.2015.2389264.

[9] S J Wei and X L Zhang and J Shi, "Sparse array microwave 3-D imaging: Compressed sensing recovery and experimental study," Progress In Electromagnetics Research, vol. 135, pp. 161–181, 2013, 10.2528/PIER12082305 .

[10] A. S. Khwaja and J. Ma, "Applications of Compressed Sensing for SAR Moving-Target Velocity Estimation and Image Compression," IEEE Transactions on Instrumentation and Measurement, vol. 60, no. 8, pp. 2848–2860, Aug. 2011, 10.1109/TIM.2011.2122190.

[11] S. Ji and Y. Xue and L. Carin, "Bayesian Compressive Sensing," IEEE Transactions on Signal Processing, vol. 56, no. 6, pp. 2346–2356, Jun. 2008, 10.1109/TSP.2007.914345.

[12] Q. Wu and Y. D. Zhang and M. G. Amin and B. Himed, "High-Resolution Passive SAR Imaging Exploiting Structured Bayesian Compressive Sensing," IEEE Journal of Selected Topics in Signal Processing, vol. 9, no. 8, pp. 1484–1497, Dec. 2015, 10.1109/JSTSP.2015.2479190.

[13] M. Zhao and H. Zhang and W. Cheng and Z. Zhang, "Joint lp- and l2,p-norm minimization for subspace clustering with outlier pursuit," 2016 International Joint Conference on Neural Networks (IJCNN), pp. 3658-3665, Jul. 2016, 10.1109/IJCNN.2016.7727670.

[14] Z. Zhang and W. Jiang and J. Qin and L. Zhang and F. Li and M. Zhang and S. Yan, "Jointly Learning Structured Analysis Discriminative Dictionary and Analysis Multiclass Classifier," IEEE Transactions on Neural Networks and Learning Systems, vol. 29, no. 8, pp. 3798-3814, Aug. 2018, 10.1109/TNNLS.2017.2740224.

[15] Z. Zhang and J. Ren and W. Jiang and Z. Zhang and R. Hong and S. Yan and M. Wang, "Joint Subspace Recovery and Enhanced Locality Driven Robust Flexible Discriminative Dictionary Learning," IEEE Transactions on Circuits and Systems for Video Technology, 2019, 10.1109/TCSVT.2019.2923007.

[16] Zhao Zhang and Weiming Jiang and Zheng Zhang and Jiahuan Ren and Sheng Li and Guangcan Liu and Jie Qin, "Scalable Block-Diagonal Locality-Constrained Projective Dictionary Learning," 28th International Joint Conference on Artificial Intelligence (IJCAI 2019), pp.4376-4382, May. 2019.

[17] Z. Zhang and F. Li and M. Zhao and L. Zhang and S. Yan, "Robust Neighborhood Preserving Projection by Nuclear/L2,1-Norm Regularization for Image Feature Extraction," IEEE Transactions on Image Processing, vol. 26, no. 4, pp. 1607-1622, Apr. 2017, 10.1109/TIP.2017.2654163.

[18] Zhao Zhang and Jiahuan Ren and Sheng Li and Richang Hong and Zhengjun Zha and Meng Wang, "Robust Subspace Discovery by Block-diagonal Adaptive Locality-constrained Representation," Proceedings of the 27th ACM International Conference on Multimedia, vol. MM '19, no. 4, pp. 1569–1577, 2019, 10.1145/3343031.3351023.

[19] Xiaojuan Huang and Li Zhang and Bangjun Wang and Zhao Zhang and Fanzhang Li, "Feature Weight Estimation based on Dynamic Representation and Neighbor Sparse Reconstruction," Pattern Recognition, vol. 81, pp. 388–403, Sep. 2018, 10.1016/j.patcog.2018.03.014.

[20] L. Zuo and Xiao-Ling and Shun-Jun and L. Dang, 'SAR 3-D imaging algorithm via Threshold Gradient Pursuit," 2017 IEEE International Geoscience and Remote Sensing Symposium (IGARSS), pp. 5370–5373, Jul. 2017, 10.1109/IGARSS.2017.8128217.

[21] Y. Zhang and D. Mao and Q. Zhang and Y. Zhang and Y. Huang and J. Yang, "Airborne Forward-Looking Radar Super-Resolution Imaging Using Iterative Adaptive Approach," IEEE Journal of Selected Topics in Applied Earth Observations and Remote Sensing, vol. 12, no. 7, pp. 2044-2054, Jul, 2019, 10.1109/JSTARS.2019.2920859.

[22] X. He and N. Tong and X. Hu, "High-Resolution Imaging and 3-D Reconstruction of Precession Targets by Exploiting Sparse Apertures," IEEE Transactions on Aerospace and Electronic Systems, vol. 53, pp. 1212–1220, Jun, 2017, 10.1109/TAES.2017.2668058.

[23] H. Liu and B. Jiu and H. Liu and Z. Bao, "Superresolution ISAR Imaging Based on Sparse Bayesian Learning," IEEE Transactions on Geoscience and Remote Sensing, vol. 52, no. 8, pp. 5005–5013, Aug, 2014, 10.1109/TGRS.2013.2286402.

[24] X. He and N. Tong and X. Hu, "Dynamic ISAR imaging of maneuvering targets based on sparse matrix recovery," Signal Processing, vol. 134, pp. 123–129, May, 2017, 10.1016/j.sigpro.2016.12.002.

[25] X. Quan and B. Guo and Y. Lu and B. Zhang and Y. Wu, "Airborne DLSLA 3-D SAR Image Reconstruction by Combination of Polar Formatting and L1 Regularization," IEEE Transactions on Geoscience and Remote Sensing, vol. 54, no. 1, pp. 213–236, Jul. 2015, 10.1109/TGRS.2015.2453202.

[26] S J Wei and X L Zhang and J Shi, "Sparse reconstruction for linear array SAR 3-D imaging based on Bayesian estimation," Proceedings of 2011 IEEE CIE International Conference on Radar, vol. 2, pp. 1522–1525, Oct, 2011, 10.1109/CIE-Radar.2011.6159851.

[27] S. Zhang and G. Dong and G. Kuang, "Superresolution Downward-Looking Linear Array three-dimensionalal SAR Imaging Based on Two-Dimensional Compressive Sensing," IEEE Journal of Selected Topics in Applied Earth Observations and Remote Sensing, vol. 9, no. 6, pp. 2184–2196, Jun, 2016, 10.1109/JSTARS.2016.2549548.

[28] S J Wei and X L Zhang and J Shi, "Sparse autofocus via Bayesian learning iterative maximum and applied for LASAR 3-D imaging," 2014 IEEE Radar Conference, pp. 666–669, May, 2014, 10.1109/RADAR.2014.6875674.

[29] X. Xiaochun and Z. Yunhua, "Fast compressive sensing radar imaging based on smoothed l0 norm," 2009 2nd Asian-Pacific Conference on Synthetic Aperture Radar, pp. 443–446, Oct, 2009, 10.1109/APSAR.2009.5374287.

[30] J. Yang and J. Thompson and X. Huang and T. Jin and Z. Zhou, "Segmented Reconstruction for Compressed Sensing SAR Imaging," IEEE Transactions on Geoscience and Remote Sensing, vol. 51, no. 7, pp. 4214–4225, Jul. 2013, 10.1109/TGRS.2012.2227060

[31] S J Wei and X L Zhang and J Shi, "Linear array SAR imaging via compressed sensing," Progress In Electromagnetics Research, vol. 117, pp. 299–319, Jan. 2011, 10.2528/PIER11033105 .

[32] Y. Zhao and B. Xiong and S. Quan and Y. Su, "Linear Array SAR Imaging Algorithm Using the Redundant Frame and Truncated SVD Based on Compressed Sensing," 2018 International Conference on Computer, Information and Telecommunication Systems (CITS), pp. 1–5, Jul, 2018, 10.1109/CITS.2018.8440179.

[33] Y. Zhang and Y. Zhang and W. Li and Y. Huang and J. Yang, "Super-Resolution Surface Mapping for Scanning Radar: Inverse Filtering Based on the Fast Iterative Adaptive Approach," IEEE Transactions on Geoscience and Remote Sensing, vol. 56, no. 1, pp. 127–144, Jan, 2018, 10.1109/TGRS.2017.2743263.

[34] Q. Zhao and G. Li and S. Xing, "FCM Algorithm Based on the Optimization Parameters of Objective Function Point," 2010 International Conference on Computing, Control and Industrial Engineering, pp. 331–333, Jun, 2010, 10.1109/CCIE.2010.200.

[35] M. Wang and A.K. Chan and C.K. Chui, "Linear frequency-modulated signal detection using Radon-ambiguity transform," IEEE Transactions on Signal Processing, vol. 46, no. 3, pp. 571–586, Mar, 1998, 10.1109/78.661326.

[36] T. Yardibi and J. Li and P. Stoica and M. Xue and A. B. Baggeroer, "Source Localization and Sensing: A Nonparametric Iterative Adaptive Approach Based on Weighted Least Squares," IEEE Transactions on

Aerospace and Electronic Systems, vol. 46, no. 1, pp. 425–443, Jan, 2010, 10.1109/TAES.2010.5417172.

[37] Z. Lu and A. M. Zoubir, "Generalized Bayesian Information Criterion for Source Enumeration in Array Processing," IEEE Transactions on Signal Processing, vol. 61, no. 6, pp. 1470–1480, Mar, 2013, 10.1109/TSP.2012.2232661.

[38] M. Ghogho and A. K. Nandi and A. Swami, "Cramer-Rao bounds and maximum likelihood estimation for random amplitude phase-modulated signals," IEEE Transactions on Signal Processing, vol. 47, no. 11, pp. 2905–2916, Nov, 1999, 10.1109/78.796427.

[39] G. H. Golub and P. C. Hansen and D. P. O'Leary, "Tikhonov Regularization and Total Least Squares," SIAM Journal on Matrix Analysis and Applications, vol. 21, no. 1, pp. 185–194, Aug, 1999, 10.1137/S0895479897326432.

[40] S. Wei and X. Zhang and J. Shi, "Compressed sensing Linear array SAR 3-D imaging via sparse locations prediction," 2014 IEEE Geoscience and Remote Sensing Symposium, pp. 1887–1890, Jul, 2014 , 10.1109/IGARSS.2014.6946825.

[41] J J Pan and Y Y Tang and B C Pan, "The algorithm of fast mean filtering," 2007 International Conference on Wavelet Analysis and Pattern Recognition, vol. 1, pp. 244–248, 2007 , 10.1109/ICWAPR.2007.4420672.

[42] R. Rovatti and M. Borgatti and R. Guerrieri, "A geometric approach to maximum-speed n-dimensional continuous linear interpolation in rectangular grids," IEEE Transactions on Computers, vol. 47, no. 8, pp. 894–899, Aug, 1998, 10.1109/12.707591.

[43] A. Maleki and D. L. Donoho, "Optimally Tuned Iterative Reconstruction Algorithms for Compressed Sensing," IEEE Journal of Selected Topics in Signal Processing, vol. 4, no. 2, pp. 330–341, Apr, 2010, 10.1109/JSTSP.2009.2039176.

[44] F. Dell'Acqua and P. Gamba, "Texture-based characterization of urban environments on satellite SAR images," IEEE Transactions on Geoscience and Remote Sensing, vol. 41, no. 1, pp. 153–159, Jan, 2003, 10.1109/TGRS.2002.807754.

[45] S. A. S. Werness and W. G. Carrara and L. S. Joyce and D. B. Franczak, "Moving target imaging algorithm for SAR data," IEEE Transactions on Aerospace and Electronic Systems, vol. 26, no. 1, pp. 57–68, Jan, 1990, 10.1109/7.53413.

[46] T. Jihua and S. Jinping and Z. Yuxi and N. Ahmad and S. Xiaoyang, "The effects of input signal-to-noise ratio on compressive sensing SAR imaging," 2010 2nd International Conference on Signal Processing Systems, vol. 3, pp. V3-533-V3-537, Jul, 2010, 10.1109/ICSPS.2010.5555816.